



1 **Carbonatite-induced petit-spot melts squeezed upward**
2 **from the asthenosphere beneath the Jurassic Pacific**
3 **Plate**

4
5 Kazuto Mikuni^{1,2*}, Naoto Hirano^{2,3}, Shiki Machida⁴, Hirochika Sumino⁵, Norikatsu Akizawa⁶,
6 Akihiro Tamura⁷, Tomoaki Morishita⁷, Yasuhiro Kato^{4,8,9}

7
8 ¹ AIST, Geological Survey of Japan, Research Institute of Geology and Geoinformation, Central 7, 1-
9 1-1, Higashi, Tsukuba, Ibaraki 305-8567, Japan.

10 ² Graduate School of Science, Tohoku University, 6-3 Aramaki-Aoba, Aoba-ku, Sendai 980-8578,
11 Japan.

12 ³ Center for Northeast Asian Studies, Tohoku University, 41 Kawauchi, Aoba-ku, Sendai 980-8576,
13 Japan.

14 ⁴ Ocean Resources Research Center for Next Generation, Chiba Institution of Technology, 2-17-1
15 Tsudanuma, Narashino 275-0016, Japan.

16 ⁵ Research Center for Advanced Science and Technology, the University of Tokyo, 4-6-1 Komaba,
17 Meguro-ku, Tokyo 153-8904, Japan

18 ⁶ Atmosphere and Ocean Research Institute, the University of Tokyo, 5-1-5, Kashiwanoha, Kashiwa
19 277-8564, Japan.

20 ⁷ Earth Science Course, Kanazawa University, Kakuma, Kanazawa 920-1192, Japan.

21 ⁸ Department of Systems Innovation, School of Engineering, The University of Tokyo, 7-3-1 Hongo,
22 Bunkyo-ku, Tokyo 113-8656, Japan.

23 ⁹ Submarine Resources Research Center, Research Institute for Marine Resources Utilization, Japan
24 Agency for Marine-Earth Science and Technology (JAMSTEC), 2-15 Natsushima-cho, Yokosuka,
25 Kanagawa, 237-0061, Japan.

26

27 * Correspondence to Kazuto Mikuni (kazuto.mikuni@aist.go.jp)

28 Authors' e-mail addresses and ORCID numbers

29 Kazuto Mikuni ^{1,2*}	kazuto.mikuni@aist.go.jp	0000-0001-6939-4333
30 Naoto Hirano ^{2,3}	nhirano@tohoku.ac.jp	0000-0003-0980-3929
31 Shiki Machida ⁴	shiki.machida@p.chibakoudai.jp	0000-0002-1069-7214
32 Hirochika Sumino ⁵	sumino@igcl.c.u-tokyo.ac.jp	0000-0002-4689-6231
33 Norikatsu Akizawa ⁶	akizawa@g.ecc.u-tokyo.ac.jp	0000-0003-4210-1160
34 Akihiro Tamura ⁷	aking826@gmail.com	0000-0002-9112-7976
35 Tomoaki Morishita ⁷	moripta@gmail.com	0000-0002-8724-6868
36 Yasuhiro Kato ^{4,8,9}	ykato@sys.t.u-tokyo.ac.jp	0000-0002-5711-8304

37

38

39



40 **Keywords: Petit-spot volcano, alkali basalt, carbonatite, asthenosphere**

41

42 **Abstract**

43

44 The lithosphere–asthenosphere boundary (LAB), which can be seismically detected, stabilizes
45 plate tectonics. Several conflicting hypotheses have been proposed as the causes of LAB discontinuity,
46 such as the contribution of hydrated minerals, mineral anisotropy, and partial melts. The petit-spot
47 melts ascending from the asthenosphere, owing to subducting plate flexures, support the partial
48 melting at the LAB. Here, we observed the lava outcrops of six monogenetic volcanoes formed by
49 petit-spot volcanism in the western Pacific. Thereafter, we determined the $^{40}\text{Ar}/^{39}\text{Ar}$ ages, major and
50 trace element compositions, and Sr, Nd, and Pb isotopic ratios of the petit-spot basalts. The $^{40}\text{Ar}/^{39}\text{Ar}$
51 ages of two monogenetic volcanoes were ca. 2.6 Ma (million years ago) and ca. 0 Ma, respectively.
52 The isotopic compositions of the western Pacific petit-spot basalts suggest their geochemically similar
53 melting sources. They were likely derived from a mixture of high- μ (HIMU) mantle-like and enriched
54 mantle (EM) -1-like components related to carbonatitic/carbonated materials and recycled crustal
55 components. A mass balance-based melting model implied that the characteristic trace element
56 composition (i.e., Zr, Hf, and Ti depletions) of the western Pacific petit-spot magmas could be
57 explained by the partial melting of garnet lherzolite with a small degree of carbonatite melt flux with
58 crustal components. This result confirms the involvement of carbonatite melt and recycled crust in the
59 source of petit-spot melts and provides an implication for the genesis of tectonic-induced volcanism
60 with similar geochemical signatures to those of petit-spots.

61

62

63 **Short Summary**

64

65 Plate tectonics theory is understood as the moving of rocky plate (lithosphere) on ductile zone
66 (asthenosphere). The causes of lithosphere–asthenosphere boundary (LAB) is controversial, but petit-
67 spot volcanism supports the presence of melt at the LAB. We analyzed chemical composition and
68 eruption age of petit-spot volcanoes on the western Pacific Plate, and the results suggested that
69 carbonatite melt and recycled oceanic crust have induced the partial melting at the LAB.

70

71 **1 Introduction**

72

73 The petrogenesis and origin of the mantle sources of alkali basalts from different tectonic
74 settings have been extensively discussed. For example, plume-related North Arch and post-erosional
75 (rejuvenated) volcanoes have been reported in Hawaii (Bianco et al., 2005; Bizimis et al., 2013; Clague



76 and Frey, 1982; Clague and Moore, 2002; Dixon et al., 2008; Frey et al., 2000; Garcia et al., 2016;
77 Yang et al., 2003). Intracontinental alkali basalts have been reported in northeastern China (e.g., Lei
78 and Zhao, 2005; Ohtani and Zhao, 2009), and the North American Basin and Range province (Axen
79 et al., 2018; Valentine and Hirano, 2010). Non-plume related intraoceanic alkali volcanoes, called
80 petit-spot volcanoes, probably originate where nearby plate subduction causes plate flexures and
81 upwelling of asthenospheric magma (Hirano et al., 2006; Hirano and Machida, 2022; Machida et al.,
82 2015, 2017; Yamamoto et al., 2014, 2018, 2020).

83 The presence of melt in the uppermost asthenosphere could be due to small-scale convection,
84 heating, or the presence of hydrous or carbonatitic components (Hua et al., 2023; Korenaga, 2020). In
85 particular, the presence of CO₂ and carbonated/carbonatitic materials is key in the formation of alkaline,
86 silica-undersaturated melt in the upper mantle (Dasgupta and Hirschmann, 2006; Dasgupta et al., 2007,
87 2013; Kiseeva et al., 2013; Novella et al., 2014). Experimental studies have shown that the solidus of
88 carbonate-bearing peridotite is lower than that of CO₂-free peridotite. In addition, the melting of
89 carbonated peridotite can produce carbonatitic and silica-undersaturated alkalic basalts (Keshav and
90 Gudfinnsson, 2013; Massuyeau et al., 2015). Primary carbonated silicate magma and evolved alkali
91 basalts have been simultaneously observed at the post-spreading ridge in the South China Sea (Zhang
92 et al., 2017; Zhong et al., 2021). Hawaiian rejuvenated volcanoes were also attributed to explained by
93 a carbonatite-metasomatized source with or without silicate metasomatism (Borisova and Tilhac,
94 2021; Dixon et al., 2008; Zhang et al., 2022).

95 Submarine petit-spot volcanoes on the subducting northwestern (NW) Pacific Plate may
96 originate from carbonate-bearing materials and crustal components (pyroxenite/eclogite) based on the
97 characteristic trace element, enriched mantle (EM)-1-like Sr, Nd, and Pb isotopic, and relatively low
98 Mg isotopic compositions (Liu et al., 2020; Machida et al., 2009, 2015). In particular, the depletion of
99 specific high-field-strength elements (HFSEs) (i.e., Zr, Hf, and Ti) and the abundant CO₂ of petit-spot
100 basalts imply that their melting sources are related to carbonatitic materials (Hirano and Machida,
101 2022; Okumura and Hirano, 2013). Here, the nature of the LAB beneath the oldest Pacific Plate aged
102 160 Ma, was characterized using the eruptive ages and geochemical properties of six newly observed
103 petit-spot volcanoes and lava outcrops. We verified the contribution of carbonatitic components and
104 crustal materials to the melting source of petit-spot volcanoes to resolve the critical question of “What
105 melts in the asthenosphere?” in this region.

106

107 **2 Background**

108

109 Petit-spots have been studied for approximately 20 years as the fourth kind of volcanic setting
110 on the Earth after mid ocean ridges, island arcs, and hotspots. These studies provide insights into the
111 nature of the upper mantle, including the oceanic lithosphere and asthenosphere, focusing on the NW



112 Pacific region (e.g., Hirano and Machida, 2022). As other implications, subducted petit-spot volcanic
113 fields with geological disturbances on the seafloor play a role in controlling the hypocentral regions
114 of megathrust earthquakes (Fujiwara et al., 2007; Fujie et al., 2020; Akizawa et al., 2022), and the
115 vestige of hydrothermal activity owing to petit-spot magmatism were recently reported (Azami et al.,
116 2023).

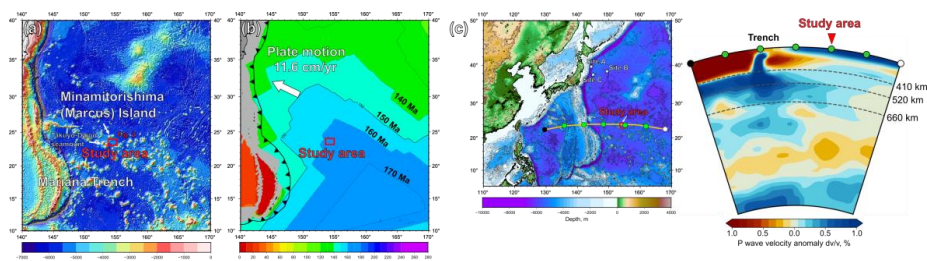
117 Considering that the mid ocean ridge basalt (MORB)-like noble-gas isotopic compositions and
118 the multiphase saturation experiments of petit-spot lavas confirm the petit-spot melts originating from
119 the asthenosphere, petit-spot volcanoes could be a key to elucidating the nature of the LAB, leading
120 to an understanding of plate tectonics (Hirano et al., 2006; Machida et al., 2015, 2017; Yamamoto et
121 al., 2018). Recently, similar volcanic activities have been observed worldwide, implying the universal
122 occurrence of petit-spot magmatism (Axen et al., 2018; Buchs et al., 2013; Falloon et al., 2022; Hirano
123 et al., 2013, 2016, 2019; Reinhard et al., 2019; Taneja et al., 2016; Uenzelmann-Neben et al., 2012;
124 Yamamoto et al., 2018, 2020; Zhang et al., 2019). Although there is still an open question of whether
125 the LAB discontinuity is due to the differences in the physical properties of minerals (e.g., Hirth and
126 Kohlstedt, 1996; Karato and Jung, 1998; Katsura and Fei, 2020; Stixrude and Lithgow-Bertelloni,
127 2005; Wang et al., 2006), presence of partial melts (e.g., Chantel et al., 2016; Conrad et al., 2011;
128 Debayle et al., 2020; Kawakatsu et al., 2009; Mierdel et al., 2007; Sakamaki et al., 2013; Yoshino et
129 al., 2006), or hybrid factor (e.g., Audhkhasi and Singh, 2022; Herath et al., 2022), the occurrence of
130 petit-spot volcanism reveals the partial melting of the asthenospheric mantle of the region (Hirano et
131 al., 2006; Hirano and Machida, 2022; Machida et al., 2015, 2017; Yamamoto et al., 2014, 2018, 2020).

132 The petit-spot volcanic province on the abyssal plain of the western Pacific is surrounded by
133 Cretaceous seamounts and oceanic islands of the Western Pacific Seamount Province (Koppers et al.,
134 2003) and located approximately 100 km southeast of the Minamitorishima (Marcus) Island (Fig. 1a).
135 The study area corresponds to the oldest portion of the Pacific Plate aged at 160 Ma and the foot of
136 the outer-rise bulge related to the Mariana subduction system (Hirano et al., 2019; Fig. 1b). Such a
137 subduction-related fore-bulge in front of the Mariana Trench has been numerically modeled and
138 detected in satellite gravity maps despite crosscutting by several seamounts (Bellas et al., 2022; Hirano
139 et al., 2019; Zhang et al., 2014, 2020). The petrography, geochemistry, and geochronology of petit-
140 spot basalts and detrital zircons in peperites, which were collected from a knoll, suggested that petit-
141 spot magmas in this region ascend from the asthenosphere along the concavely flexed plate in response
142 to subduction into the Mariana Trench at younger than ~ 3 Ma (Yamamoto et al., 2018; Hirano et al.,
143 2019). Below the study area, low seismic velocity zone was observed under the lithosphere (Fig. 1c).
144 Although the low velocity anomalies crosscutting the lower mantle, no active hotspots have been
145 reported around the western Pacific petit-spot province (Fig. 1c). The other petit-spot lava outcrops
146 were observed in a volcanic cluster during three research cruises using the research vessel (RV)
147 *Yokosuka* (YK16-01, YK18-08, and YK19-05S) with five dives using the submersible, *Shinkai 6500*



148 (6K#1466, 6K#1521, 6K#1522, 6K#1542, and 6K#1544; Fig. 2), and fresh basalts were collected. The
 149 information of sampling point, depth, thickness of palagonite rind and manganese-crust, and age of
 150 the western Pacific petit-spot basalts were provided in Table 1.

151



152

153 Fig. 1. Geological and geophysical information of the study area. (a) Bathymetry of the western Pacific near the
 154 Mariana Trench. The red box shows the study area to the southeast of Minamitorishima (Marcus) Island
 155 (Fig. 2). The bathymetric data are adopted from ETOPO1 (NOAA National Geophysical Data Center;
 156 <http://www.ngdc.noaa.gov/>). (b) Seafloor age map of the same area as (a). This study area is on a 160–
 157 170 Ma Pacific Plate, called the Jurassic Quiet Zone (JQZ) (Tivey et al. 2006). The present absolute
 158 motion of the Pacific Plate and the seafloor age were derived from studies by Gripp and Gordon (1990)
 159 and Müller et al. (2008), respectively. (c) The cross-section P-wave tomography beneath the thick white
 160 line including the study area on the ETOPO1 bathymetry map (left). The tomographic image (right) was
 161 drawn using the SubMachine (Hosseini et al., 2018;
 162 <http://www.earth.ox.ac.uk/~smachine/cgi/index.php>) on applying the data of Lu et al. (2019).

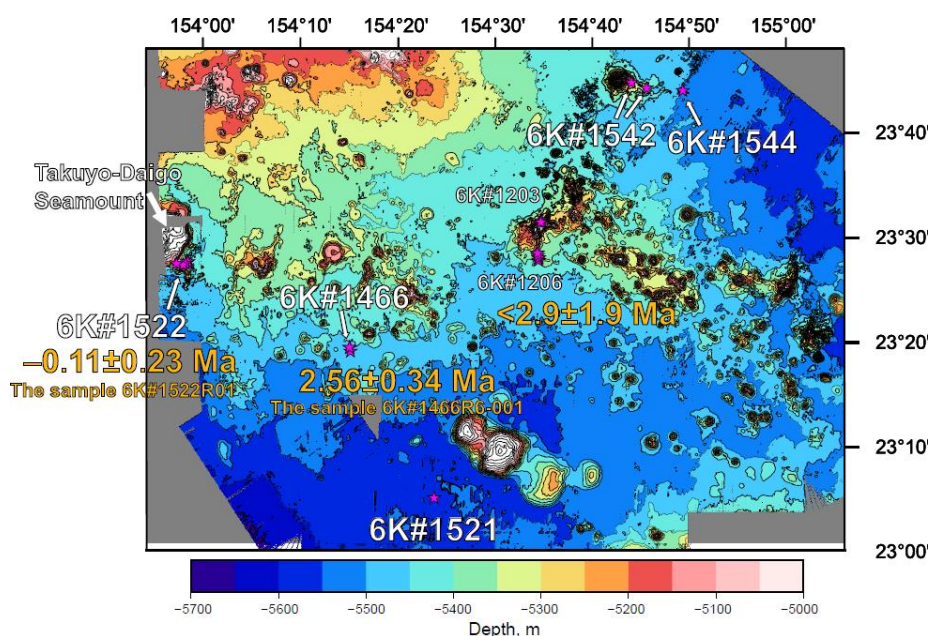
Table 1
 Information of the collected western Pacific petit-spot basalts

Cruise	Dive	Sample name	Latitude (N)	Longitude (E)	Depth, m	Palagonite rind, mm *1	Manganese crust, mm *1	Ar-Ar age, Ma		
YK16-01	6K#1466	R3-001	23° 19.1009	154° 15.0950	5453	4.45	7.155	2.56±0.34		
		R3-04	23° 19.1009	154° 15.0950	5453	3.005	5.805			
		R6-001	23° 19.4475	154° 15.0367	5300	6.61	5.205			
		R7-001	23° 19.4713	154° 15.0000	5267	5.54	4.31			
		R7-003	23° 19.4713	154° 15.0000	5267	-	-			
		R7-003	23° 19.4713	154° 15.0000	5267	-	-			
YK18-08	6K#1521	R04	23° 5.0880	154° 23.7360	5546	1.045	5.935	-0.11±0.23 ^{*2}		
		R05	23° 5.0880	154° 23.7360	5546	-	5.625			
	6K#1522	R01	23° 27.6420	153° 58.3140	5300	6.015	5.78			
		R02	23° 27.6420	153° 58.3140	5300	4.505	2.66			
		R03	23° 27.6420	153° 58.3140	5300	5.44	4.04			
		R05	23° 27.6360	153° 58.3080	5294	2.92	4.785			
		R12	23° 27.4920	153° 58.0620	5189	6.05	5.56			
		R13	23° 27.4920	153° 58.0620	5189	4.545	5.895			
		R14	23° 27.3540	153° 57.8160	5303	2.04	5.475			
		R16	23° 27.4680	153° 57.1200	5182	3.825	3.845			
		R17	23° 27.4680	153° 57.1200	5182	5.19	5.67			
		YK19-05S	6K#1542	R03	23° 44.1926	154° 45.6900	5359		3.43	4.26
				R05	23° 44.1926	154° 45.6900	5359		3.245	4.355
				R06	23° 44.7064	154° 44.1200	5190		-	-
R09	23° 44.7064			154° 44.1200	5190	-	-			
6K#1544	R04			23° 43.9555	154° 49.4277	5488	4.39	4.955		
	R05			23° 43.9555	154° 49.4277	5488	2.965	4.97		
		R06	23° 43.9555	154° 49.4277	5488	3.425	5.82			

* 1: The samples which have no data of palagonite and/or Mn-crust thickness are due to the lack of them or crumbled.

* 2: This is a reference value due to the lack of radiogenic ⁴⁰Ar in this sample.

163



164

165

Fig. 2. Detailed bathymetry of the study area. The onboard multibeam data were surveyed during the YK10-05 and the YK18-08 cruises by the Japan Agency for Marine-Earth Science and Technology (JAMSTEC). The petit-spot knolls and outcrops were investigated during several dives as 6K#1466, 6K#1521, 6K#1522, 6K#1542, and 6K#1544. The pink-colored stars represent the sampling points. The age information was obtained in the present study and Hirano et al. (2019).

167

168

169

170

171

3 Field observations, sample locations, and petrography

172

173

174

Here, the eruptive sites of monogenetic volcanoes or lava outcrops were approximately along each dive site numbered 6K#1466, #1521, #1522, #1542, and #1544 conducted using the *Shinkai 6500*. Only the 6K#1466 dive was conducted at two types of monogenetic volcanoes, divided into the glassy (R3) and crystalline, vesicular (R6 and R7) types based on the geochemical and petrographic descriptions and occurrence of basaltic samples.

177

178

179

3.1 YK16-01 cruise and 6K#1466 dive

180

181

182

During the YK16-01 cruise, a small conical knoll (ca. 0.04 km³) was investigated by a submersible dive, 6K#1466 (Figs. 2 and 3a). The lava flows, observed hollow lava tube resulting in sediment-rolling/disturbing eruption, were located approximately 600 m south of the top of the knoll

183

184



185 (extremely fresh and glassy samples; 6K#1466R3-001 and R3-004 basalts) (Fig. 3a). Vesicular pillow
186 basalts were collected on the western slope of the knoll (samples 6K#1466R6-001, R7-001, and R7-
187 003; Fig. 3a). Although only the strong acoustic reflection could not completely distinguish the petit-
188 spot lava fields in ferromanganese nodule fields, this dive revealed lava outcrops using a sub bottom
189 profiler (SBP) and a multi narrow beam echo sounder (MBES). In detail, the petit-spot lava field, as
190 an acoustically opaque layer, was identified by a vigorous backscattering intensity in the MBES with
191 the distributions of the basement and sediment layers in the SBP.

192 The 6K#1466R3-001 and R3-004 samples were extremely fresh glassy basalts. The R3-001 and
193 R3-004 basalts exhibited similar petrographic features (Fig. 3a). These basalts were covered by 3.0–
194 4.5 mm-thick palagonite (hydrated quenched glass), and their outermost parts were surrounded by
195 5.8–7.2 mm-thick ferromanganese crust (Fig. 3a). They were less vesicular (<3 vol.%) and dominantly
196 basaltic glass with euhedral–subhedral olivine microphenocrysts (~100–500 μm in size), ferrotitanium
197 oxide (<50 μm in size), and minor plagioclase (~500 μm in size) (Fig. 3a).

198 The 6K#1466R6-001, R7-001, and R7-003 basalts, covered with 4.3–5.2 mm-thick
199 ferromanganese crust over 5.5–6.6 mm-thick palagonite rinds, exhibited high vesicularity (20–40
200 vol.%) (Fig. 3a). Certain pyroxene-dominated xenocrysts and peridotite xenoliths have been reported
201 by Mikuni et al. (2022). The basaltic groundmass comprised needle-shaped clinopyroxene (50–400
202 μm in size), subhedral olivine partly with aureoles of iddingsite (up to 100 μm in size), ferrotitanium
203 oxide, spinel (up to 10 μm in size), glass, and crystallite, notably without remarkable phenocrysts (Fig.
204 3a). The photomicrograph of R6-001 is shown in Fig. 3a.

205

206 **3.2 YK18-08 cruise and 6K#1521 and #1522 dives**

207

208 Two submersible dives (6K#1521 and 1522) were conducted during the YK18-08 cruise to
209 investigate petit-spot volcanoes. During the 6K#1521 dive, a small lava outcrop was discovered in the
210 abyssal plain by tracing the strong acoustic reflection, which was expectedly derived from intrusive
211 rock bodies, in the sedimentary layer detected by deep-sea SBP equipped on the *Shinkai* 6500. We
212 observed that the strong reflective surface gradually became shallow during the navigation, revealing
213 the small lava outcrop (Figs. 2 and 3b). Fresh and massive (nonvesicular) basalts were collected from
214 this outcrop (samples 6K#1521R04 and R05; Fig. 3b). The samples from the 6K#1522 dive at a
215 seamount exhibited highly irregular shapes, and massive lava flows, pillows, and lava breccia were
216 observed (Fig. 3c). All the samples were fresh vesicular basalts (6K#1522R01, R02, R05, R12, R13,
217 R16, and R17; Fig. 3c).

218 The fresh, massive, and nonvesicular basalts were obtained by 6K#1521 dive (R04 and R05)
219 comprised euhedral olivine microphenocrysts (150–400 μm in size), two types of ferrotitanium oxide
220 (50–150 μm in size), and crystallite (Fig. 2b). They were covered with 5.6–5.9 mm-thick



221 ferromanganese crust and ~ 1.0 mm-thick palagonite rinds (Fig. 3b), but R05 did not have palagonite
222 rinds. The photomicrograph of R04 is shown in Fig. 3b.

223 The seven fresh basalts collected during the 6K#1522 dive (6K#1522R01, R02, R05, R12, R13,
224 R16, and R17), exhibited high vesicularity (20–40 vol.%) with 2.9–6.0 mm-thick palagonite rinds
225 covered with 2.7–5.9 mm-thick ferromanganese crusts (Fig. 3c). Euhedral–subhedral olivine
226 microphenocrysts (glomeroporphyritic, 30–200 μm in size), radial–needle-shaped clinopyroxene,
227 iddingsite (<200 μm in size), spinel, and glass with minor xenocrystic olivines were observed (Fig.
228 3c). The photomicrograph of R01 is shown in Fig. 3c.

229

230 **3.3 YK19-05S cruise and 6K#1542 and #1544 dives**

231

232 A petit-spot knoll and related lava flows were surveyed by the 6K#1542 and #1544 dives,
233 respectively, during the YK19-05S cruise (Fig. 2). During the 6K#1542 dive, geological survey and
234 rock sampling were conducted from two points on the eastern slope of the knoll (Figs. 2 and 3d). Here,
235 the 6K#1542R03 and R05 basalts were collected from the lava-breccia field covered with thin
236 ferromanganese crust (Fig. 3d). Samples R06 and R09 were obtained from the lobate-surface lava
237 between tubular lavas closer to the summit than R03 and R05 (Fig. 3d).

238 High-resolution (one-meter scale) bathymetric mapping was successfully conducted during the
239 6K#1544 dive, and this can contribute to future oceanographic investigations using the Human
240 Occupied Vehicle (Kaneko et al., 2022). During this acoustic survey, several mounds, 10–20 m in
241 height and a few hundred meters in diameter, were recognized (Fig. 3d). We observed these mounds
242 and collected samples from outcrops during the second half of the dive. Pillow lavas, tumuli, and lava
243 breccias were observed, and basaltic samples (6K#1544R04, R05, and R06) were collected (Fig. 3d).

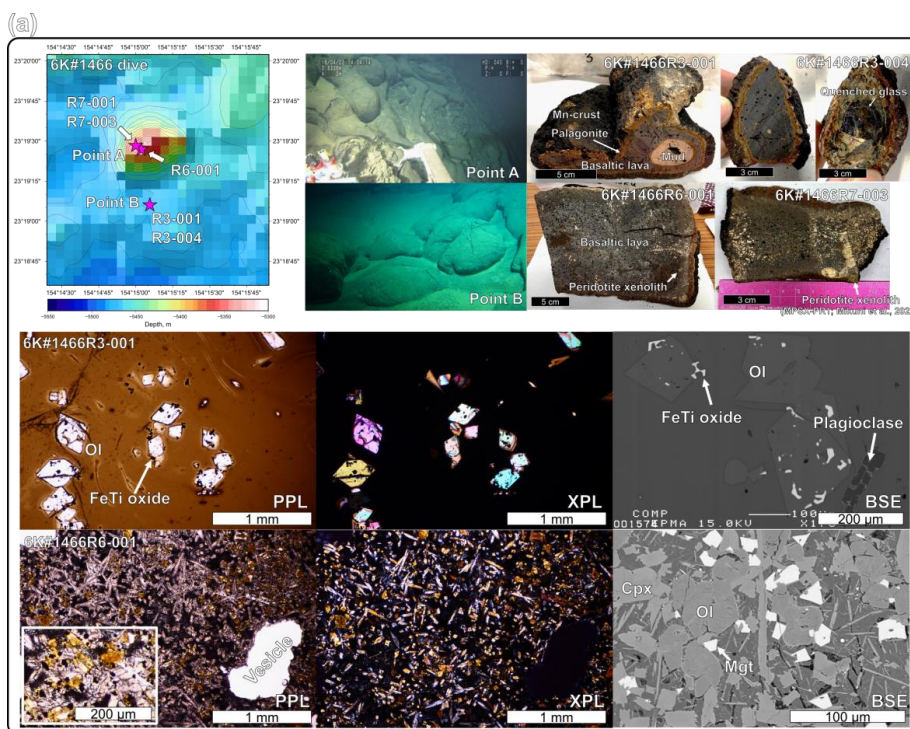
244 Four vesicular basalts (10–30 vol.% vesicularity; 6K#1542R03, R05, R06, and R09) were
245 covered with 4.3–4.4 mm-thick ferromanganese crust. The outer palagonitic rinds were 3.2–3.4 mm-
246 thick (Fig. 3d). A few to 300- μm -sized euhedral–subhedral olivine microlites and microphenocrysts
247 were glomeroporphyritic (Fig. 3d). The groundmass was dominated by needled dendritic
248 clinopyroxenes (~100 μm in size). The others were olivine, spinel, glass, and xenocrystic olivine
249 megacrysts. The photomicrograph of R06 is shown in Fig. 3d.

250 The basaltic samples from the 6K#1544 dive (6K#1544R04, R05, and R06) were covered with
251 ferromanganese crust (5.0–5.8 mm-thick) over palagonitic rinds (3.4–4.4 mm-thick). All the samples
252 exhibited high vesicularity in the range of 20–35 vol.% (Fig. 3d). They comprised olivine
253 microphenocrysts (30–250 μm in size, euhedral–subhedral or columnar), clinopyroxene (<100 μm ,
254 needled, columnar, radial or dendritic shape), spinel, and glass (Fig. 3d). The photomicrograph of R04
255 is shown in Fig. 3d. During macroscopic observations, practically all the basalts from the 6K#1542
256 and 6K#1544 dives exhibited similar vesicularity and freshness. Their geochemical features were also

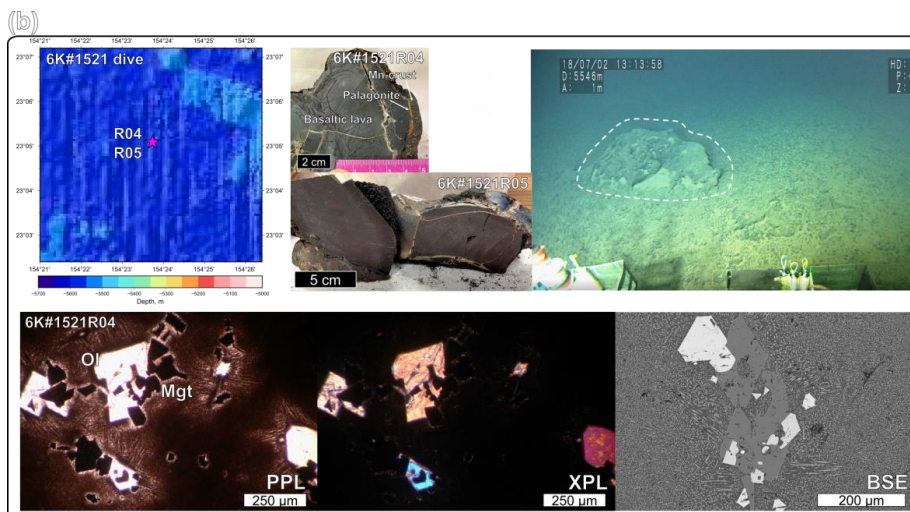


257 similar to each other and are described in Sect. 5-1 and 5-2.

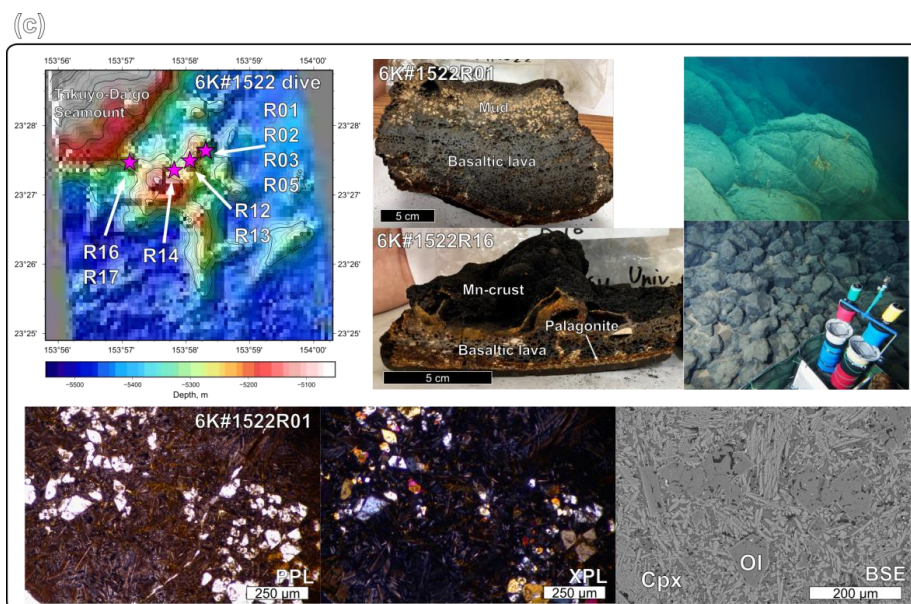
258



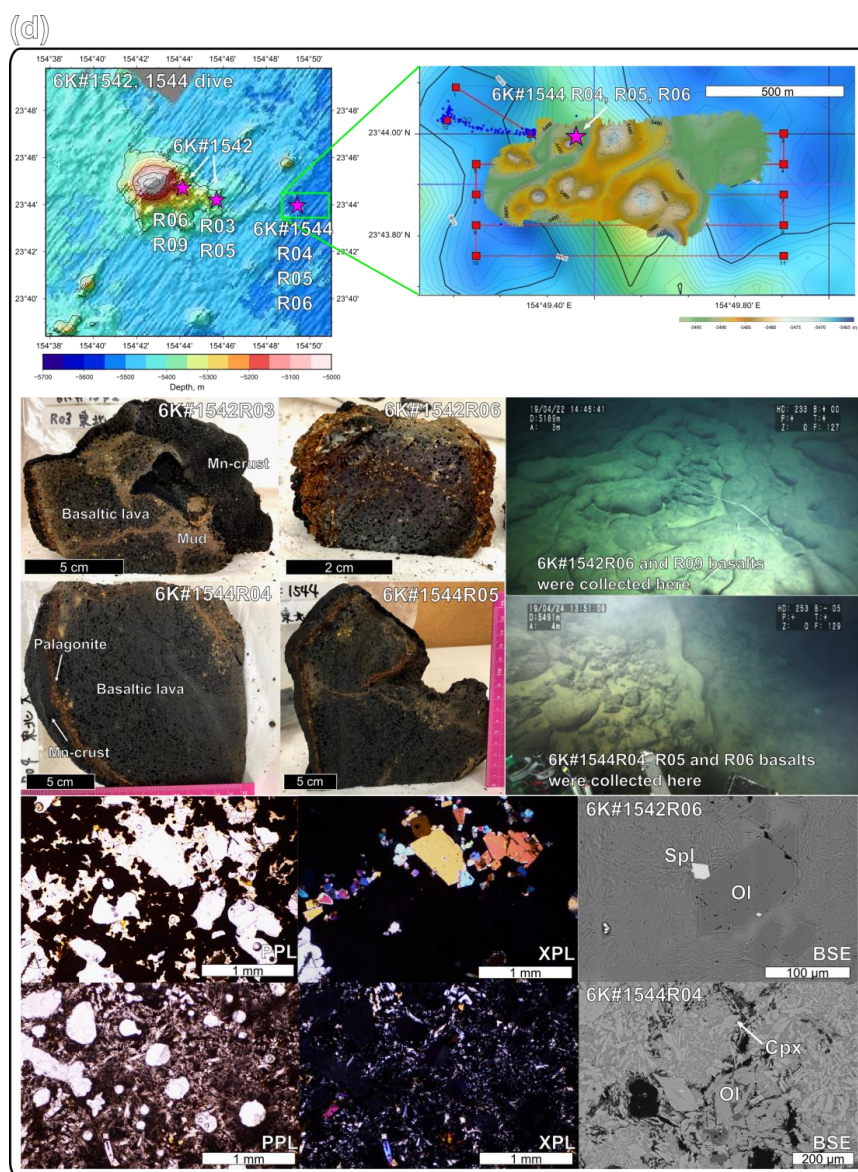
259



260



261



262
 263 Fig. 3. Bathymetric map with photos of the outcrop, the collected samples, and their photomicrographs with detailed
 264 bathymetry of the sampling points. (a) The 6K#1466, (b) 6K#1521, (c) 6K#1522, and (d) 6K#1542 and
 265 6K#1544 dives using the *Shinkai 6500* by JAMSTEC. The 1-m gridded bathymetry of the 6K#1544 dive
 266 is shown in (d), obtained using an MBES equipped with the *Shinkai 6500* over a 100-m resolution map
 267 obtained using the surface ship, R/V *Yokosuka* (Kaneko et al., 2022). The photomicrographs of
 268 representative samples are shown for plane-polarized light (PPL), cross-polarized light (XPL), and



269 backscatter electron (BSE). Ol, olivine; Cpx, clinopyroxene; Mgt, magnetite; Spl, spinel.

270

271

272 **4. Analytical methods**

273

274 **4.1 Major and trace element analysis of volcanic glass and whole-rock**

275

276 Major element compositions of glasses were determined using an electron probe micro analyzer
277 (EPMA; JXA-8900R) at Atmosphere and Ocean Research Institute (AORI), the University of Tokyo.
278 The analyses were performed using an accelerating voltage of 15 kV, a beam current of 12 nA, and a
279 beam diameter of 10 μm . A peak counting time of 20 s and a background counting time of 10 s were
280 used, except for Na and Ni, for which a peak counting time of 5s and 30 s and a background counting
281 time of 2s and 15 s were used, respectively. Natural and synthetic minerals were used as standards
282 (Akizawa et al., 2021).

283 The trace element compositions of minerals were determined using a laser ablation-inductively
284 coupled plasma-mass spectrometry (LA-ICP-MS; New Wave Research UP-213 and Agilent 7500s) at
285 Kanazawa University. The Nd: YAG deep UV (ultraviolet) laser's wavelength is 213 nm. The analyses
286 were conducted with 100 μm spot size. A repetition frequency of 6 Hz and a laser energy density of 8
287 J cm^{-2} were used. NIST612 glass (distributed by National Institute of Standards and Technology) was
288 employed for calibration, using the preferred values of Pearce et al. (1997). Data reduction was
289 undertaken with ^{29}Si as the initial standard, and SiO_2 concentrations were obtained by an electron
290 microprobe analysis (Longerich et al., 1996). BCR-2G (distributed by the United States Geological
291 Survey) was used as a secondary standard to assess the precision of each analytical session (Jochum
292 and Nohl, 2008).

293 Whole-rock major and trace element compositions of rock samples were analyzed by Activation
294 Laboratories Ltd., Canada, using Code 4Lithoresearch Litho geochemistry and ultratrace5 Exploration
295 Geochemistry Package. The former package uses lithium metaborate/tetraborate fusion with
296 inductively coupled plasma optical emission spectrometry (FUS-ICP-OES) and inductively coupled
297 plasma mass spectrometry (FUS-ICP-MS) for the major and trace element analyses, respectively. The
298 latter package uses inductively coupled plasma optical emission spectrometry (ICP-OES) and
299 inductively coupled plasma mass spectrometry (ICP-MS) for the major and trace element analyses,
300 respectively.

301

302 **4.2 Sr, Nd, and Pb isotope analysis**

303

304 **4.2.1 Acid leaching**



305

306 Acid leaching was conducted for the selected basaltic samples on the basis of the procedure of
307 Weis and Frey (1991, 1996) as follows: [1] About 0.3–0.4 or 0.6 g of rock powder is weighed into an
308 acid-washed 15 mL Teflon vial (Savilex®). [2] 10 or 12 mL of 6N (N: normality) HCl were added, and
309 then heated at 80°C for 20–30 min. [3] After heating, the suspension is ultra-sonicated in 60°C water
310 for 20 min. [4] The supernatant is decanted. Steps [2] to [4] were repeated more than 4 times (up to 6
311 times) until the supernatant become clear or pale yellow to colorless. [5] TAMAPURE-AA Ultrapure
312 water (Tama Chemicals; Co., Ltd.), which includes a lower Pb blank than milli-Q H₂O, were added
313 instead of 6N HCl, and the suspension is ultra-sonicated for 20 min. This step is conducted twice. [6]
314 The leached rock powder is dried on a hot plate at 120°C. [7] After cooling, the powder is weighed.

315

316 **4.2.2 Extraction of Pb, Sr, and Nd**

317

318 The extraction of Pb, Sr, and Nd was performed following the procedures of Tanimizu and
319 Ishikawa (2006) and Machida et al. (2009). First, from ~50 to ~100 mg of rock powder was weighted
320 in a 7 mL Teflon vial (designated as “vial A”), and digested using mixed acid composed of HF and
321 HBr. The separation was conducted by cation exchange resin (AG-1X8; Bio-Rad Laboratories Inc.)
322 on the basis of procedures described in Tanimizu and ishikawa (2006). All fractions from the first and
323 second supernatant loading (0.5 M HBr) to the elution of other elements (mixed acid composed of
324 0.25 M HBr and 0.5 M HNO₃) were collected in another 7 mL Teflon vial (designated as “vial B”) for
325 Sr and Nd separation. Finally, Pb was extracted by 1 mL of 1M HNO₃ in another 7 mL Teflon vial
326 (designated as “vial C”). The procedural blanks for Pb totaled less than 23 pg.

327 The Sr and Nd-bearing solution in the vial B was transferred into the vial A containing residues
328 of digested samples. 2 mL of HClO₄ and 2 mL HNO₃ was further added to the vial A, and the residue
329 was dissolved at 110 °C. The Sr and Nd were separated by column with a cation exchange resin
330 (AG50W-8X; Bio-Rad Laboratories Inc.) and a Ln resin (Eichrom Technologies Inc.) on the basis of
331 procedures described in Machida et al. (2009). The separated Sr and Nd were further purified by
332 column separation with a cation exchange resin. The total procedural blanks for Sr and Nd were less
333 than 100 pg.

334

335 **4.2.3 Analytical procedure**

336

337 Pb isotopic ratios were obtained using the multi-collector ICP-MS (MC-ICP-MS; Neptune plus,
338 Thermo Fisher Scientific), with nine Faraday collectors, at Chiba Institute of Technology (CIT), Japan.
339 The NIST SRM-981 Pb standard was also analyzed and yielded the average values of ²⁰⁶Pb/²⁰⁴Pb =
340 16.9303 ± 0.0005, ²⁰⁷Pb/²⁰⁴Pb = 15.4828 ± 0.0006, and ²⁰⁸Pb/²⁰⁴Pb = 36.6710 ± 0.0016. These



341 correspond to previous values determined using MC-ICP-MS with Tl normalization, but they were
342 slightly lower than values determined by TIMS in Tanimizu and Ishikawa (2006) from the ^{207}Pb – ^{204}Pb
343 double-spike. Reproducibility was monitored by an analyses of the JB-2 GSJ standard, and the
344 obtained value was $^{206}\text{Pb}/^{204}\text{Pb} = 18.3326 \pm 0.0005$, $^{207}\text{Pb}/^{204}\text{Pb} = 15.5453 \pm 0.0006$, and $^{208}\text{Pb}/^{204}\text{Pb}$
345 $= 38.2240 \pm 0.0017$.

346 Sr and Nd isotopic analyses for powdered rocks and glasses were conducted using the thermal
347 ionization mass spectrometry (TIMS; Triton XT, Thermo Fisher Scientific) with nine Faraday
348 collectors, at CIT. 1.5 μL of 2.5M HCl and 0.5M HNO_3 was used for loading of separated Sr and Nd
349 of sample on the single and double Re-filament, respectively. The measured isotopic ratios were
350 corrected for instrumental fractionation by adopting the $^{86}\text{Sr}/^{85}\text{Sr}$ value to be 0.1194 and that of
351 $^{146}\text{Nd}/^{144}\text{Nd}$ to be 0.7219. The average value for the NIST SRM-987 Sr standard was 0.710239
352 ± 0.000005 (2σ , $n=2$), and that for the GSJ JNdi-1 Nd standard was 0.512103 ± 0.000005 (2σ , $n=2$).
353 They agree well with values from the literature for the NIST SRM-987 ($^{87}\text{Sr}/^{86}\text{Sr} = 0.710252$ –
354 0.710256 ; Weis et al., 2006) and JNdi-1 ($^{143}\text{Nd}/^{144}\text{Nd} = 0.512101$; Wakaki et al., 2007). Consequently,
355 we did not correct the values of the unknowns for offsets between the measurements and the values
356 for the Sr and Nd standards.

357

358 **4.3 $^{40}\text{Ar}/^{39}\text{Ar}$ dating**

359

360 Samples for $^{40}\text{Ar}/^{39}\text{Ar}$ dating were prepared by separating crystalline groundmass after crushing
361 them to sizes between 100 and 500 μm . The separated groundmass samples were leached by HNO_3 (1
362 mol/L) for one hour to remove clays and altered materials. All samples were wrapped in aluminum
363 foil along with JG-1 biotite (Iwata, 1998), K_2SO_4 , and CaF_2 flux monitors. Any amorphous (e.g.,
364 quenched glass) was removed because ^{39}Ar may move from one phase to another in a process known
365 as “recoil.” This can create a disturbed age spectrum when ^{39}Ar is produced from ^{39}K in amorphous
366 material through interaction with fast neutrons during irradiation of the sample. Samples were
367 irradiated for 6.6 days in the Kyoto University Research Reactor (KUR), Kyoto University. Argon
368 extraction and isotopic analyses were undertaken at the Graduate School of Arts and Sciences, the
369 University of Tokyo. The sample gases were extracted by incremental heating of 10 or 11 steps
370 between 600°C and 1500°C. The analytical methods used are the same as those used by Ebisawa et al.
371 (2004) and Kobayashi et al. (2021).

372

373 **4.4 Geochemical modeling**

374

375 The partial melting model was established using the open-system mass balance modeling
376 (OSM-4) of Ozawa et al. (2001), referring the parameters of Borisova and Tilhac (2021). This model



377 was based on the mass conservation equations of one-dimensional steady-state melting. In the model
378 in this study, the critical melt fraction (α_c ; mass fraction of melt when melt separation begins = melt
379 connectivity threshold) was fixed at 0.01. The system was opened to fluxing at a constant melt-
380 separation rate (γ) when the system reached the α_c . The final trapped melt fraction (α_f ; mass fraction
381 of melt trapped in the residue) was also fixed at ~ 0 (it was calculated as 10^{-6} owing to mass balance).
382 We calculated the trace element composition of partial melts at various degree of melting (F), rate of
383 influx (β) and melt separation (γ). We assumed a primitive mantle (PM) source as a lherzolite with or
384 without a normal (N)-MORB source as the recycled oceanic crust (Sun and McDonough, 1989), such
385 as pyroxenite and eclogite. The recycled crust (N-MORB component) was mixed in the source as
386 compositional heterogeneity calculated as “0.05N-MORB + 0.95PM” for the trace element
387 concentration, and the considered mineral phases and their proportions were derived only from garnet
388 lherzolite (i.e., olivine, orthopyroxene, clinopyroxene, and garnet). The mineral mode of garnet
389 lherzolite (olivine 55%, orthopyroxene 20%, clinopyroxene 15%, and garnet 10%) and the melting
390 reaction mode (olivine 8%, orthopyroxene –19%, clinopyroxene 81%, and garnet 30%) were based
391 on studies by Johnson et al. (1990) and Walter (1998), respectively. In this situation, the clinopyroxene
392 was consumed at an F (degree of partial melting) of $\sim 19\%$; therefore, the system was calculated up
393 to 18% partial melting. The carbonatite melt, as an influx, in this model was “average carbonatite”
394 from a study by Bizimis et al. (2003). The partition coefficient of trace elements was generally based
395 on a study by McKenzie and O’Nions (1991) excluding Y (White, 2013), and Ti for clinopyroxene
396 and garnet (Kelemen et al., 2003). The variables of β (influx rate) and γ (melt-separation rate) were
397 changed during the modeling within the mass balance ($\gamma \leq \beta + 1$). The modeled melts were outputted
398 as “total melt,” considering the instantaneous and accumulated melts. Non-modal batch melting for
399 garnet lherzolite was also performed using the same parameters and Shaw (1970)’s equation.

400

401 **5 Results**

402

403 To describe the geochemical and chronological results, each sample group was denoted by its
404 dive number, e.g., the sample group obtained from the 6K#1521 dive was labeled “1521 samples”.
405 The basalts from the 6K#1466 dive were divided into two groups for R3 (collected from the seafloor
406 south of the knoll) and R6–R7 (sampled on the knoll) based on their geographical, petrological, and
407 compositional differences. The mineral compositions of each petit-spot basalt are shown in Fig. S1
408 and Table S1.

409

410 **5.1 Major and trace element compositions**

411

412 The major and trace element compositions for the whole rock and glass of the petit-spot basalts



413 are listed in Table 2. The basalt compositions for a petit-spot knoll were reported by Hirano et al.
414 (2019) (expressed as “1203, 1206” in each figure). The data are discussed along with the reported NW
415 Pacific petit-spots (Hirano and Machida, 2022). Using a total alkali vs. silica (TAS) diagram, virtually
416 all the samples were classified as alkalic rocks, but the 1542 and 1544 basalts were plotted near the
417 boundary between alkalic and non-alkalic (Fig. 4a). Two petit-spot basalts (1466R7-001 and R7-003)
418 from the petit-spot knoll were notably silica-undersaturated (i.e., $\text{SiO}_2 = 39.3\text{--}39.4$ wt%) and classified
419 as foidite (Mikuni et al., 2022). All the western Pacific petit-spot basalts, except for the 6K#1466R7
420 basalts, were sodic ($\text{K}_2\text{O}/\text{Na}_2\text{O} = 0.24\text{--}0.58$), and were notably discriminated to those of the NW
421 Pacific petit-spots (Fig. 4b).

422 Selected major element oxides and trace element ratios vs. MgO plots for the petit-spot basalts
423 are shown in Figs. 5 and 6, respectively. The MgO concentrations of the 1466R3 and 1521 samples
424 each exhibiting similar petrographic features (i.e., nonvesicular, and glassy) were characterized by
425 values (4.0–4.4 wt%) lower than those of other vesicular samples (6.6–9.3 wt%). The K_2O , Na_2O ,
426 Al_2O_3 , and SiO_2 contents negatively correlated with MgO (Figs. 5a–d). The CaO, FeO_T , and
427 $\text{CaO}/\text{Al}_2\text{O}_3$ abundances exhibited positive correlations with MgO (Figs. 5e–g). The TiO_2
428 concentrations exhibited no correlations with MgO (Fig. 5h), as well as the selected trace element
429 ratios (Figs. 6a–g) except for the Sm/Hf ratio with positive correlations (Fig. 6h). The Sm/Hf ratio also
430 negatively correlated with SiO_2 (Fig. S2).

431 The PM-normalized (Sun and McDonough, 1989) trace element patterns for the petit-spot
432 basalts, including those reported by a previous study (Hirano et al., 2019), were shown for each dive
433 with the representative ocean island basalt (OIB) in Figs. 7a–f. The petit-spot basalts generally showed
434 high light rare earth element (LREE)/heavy REE (HREE) ratios. Negative Zr, Hf, Ti, and Y anomalies
435 were commonly observed in these western Pacific petit-spots as well as those of the NW Pacific petit-
436 spots (Fig. 7g). The 1466 basalts collected on the seafloor south of the knoll (6K#1466R3-001 and
437 R3-004) were compositionally different from those obtained on the knoll (6K#1466R7-001, R7-003).
438 The basalts from the 6K#1542 and 1544 dives, collected from nearby locations, had the same
439 compositions in major and trace element ratios in both whole rock and glass, respectively (Figs. 4, 5,
440 6, 7e, and f). These samples in the Ba/Nb and Sm/Hf diagrams were plotted in the range of “Group 3”
441 in the discrimination of the NW Pacific petit-spot basalts (Machida et al., 2015), indicating their
442 negative Zr and Hf anomalies without notable U, Th, Nb, and Ta anomalies in the PM-normalized
443 trace element patterns (Fig. 7h). The Sm/Hf ratio of the differentiated 1466R3 samples was lower than
444 that of other samples. A positive correlation between fluid mobile and immobile elements, Ba vs. Nb
445 (Fig. 8a) and U vs. Th (Fig. 8b), respectively, was observed, excluding the Ba of the 1466R7 samples
446 (Fig. 8a).

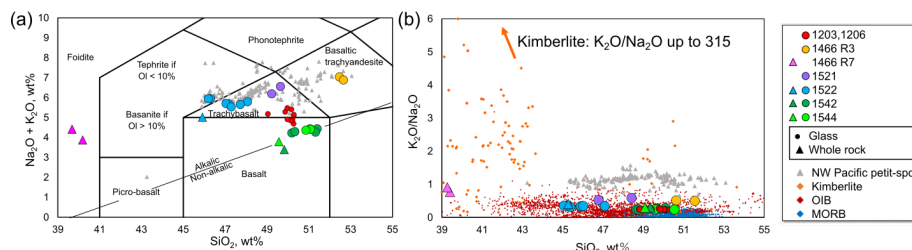


Table 2
 Major cation element concentrations of ambient Particulate Matter (PM)₁₀ samples

Sample name: 04/14/08/01 04/14/08/02 04/14/08/03 04/14/08/04 04/14/08/05 04/14/08/06 04/14/08/07 04/14/08/08 04/14/08/09 04/14/08/10 04/14/08/11 04/14/08/12 04/14/08/13 04/14/08/14 04/14/08/15 04/14/08/16 04/14/08/17 04/14/08/18 04/14/08/19 04/14/08/20 04/14/08/21 04/14/08/22 04/14/08/23 04/14/08/24 04/14/08/25 04/14/08/26 04/14/08/27 04/14/08/28 04/14/08/29 04/14/08/30 04/14/08/31

Element	01	02	03	04	05	06	07	08	09	10	11	12	13	14	15	16	17	18	19	20	21	22	23	24	25	26	27	28	29	30	31
K ₂ O	51.96	39.40	39.40	46.38	46.38	46.38	46.38	46.38	46.38	46.38	46.38	46.38	46.38	46.38	46.38	46.38	46.38	46.38	46.38	46.38	46.38	46.38	46.38	46.38	46.38	46.38	46.38	46.38	46.38	46.38	46.38
CaO	14.99	15.10	11.41	15.12	14.38	12.74	12.48	11.99	12.91	13.08	12.65	12.55	12.55	12.55	12.55	12.55	12.55	12.55	12.55	12.55	12.55	12.55	12.55	12.55	12.55	12.55	12.55	12.55	12.55	12.55	12.55
MgO	0.00	0.00	0.00	0.00	0.00	0.00	0.00	0.00	0.00	0.00	0.00	0.00	0.00	0.00	0.00	0.00	0.00	0.00	0.00	0.00	0.00	0.00	0.00	0.00	0.00	0.00	0.00	0.00	0.00	0.00	0.00
SiO ₂	7.07	7.07	7.07	7.07	7.07	7.07	7.07	7.07	7.07	7.07	7.07	7.07	7.07	7.07	7.07	7.07	7.07	7.07	7.07	7.07	7.07	7.07	7.07	7.07	7.07	7.07	7.07	7.07	7.07	7.07	7.07
Al ₂ O ₃	7.04	3.90	1.34	1.08	8.43	7.36	1.78	1.25	1.78	1.25	1.78	1.25	1.78	1.25	1.78	1.25	1.78	1.25	1.78	1.25	1.78	1.25	1.78	1.25	1.78	1.25	1.78	1.25	1.78	1.25	1.78
Fe ₂ O ₃	4.61	4.38	2.15	2.29	3.36	4.05	4.16	4.01	4.16	4.01	4.16	4.01	4.16	4.01	4.16	4.01	4.16	4.01	4.16	4.01	4.16	4.01	4.16	4.01	4.16	4.01	4.16	4.01	4.16	4.01	4.16
NiO	0.31	2.24	1.65	1.08	0.26	2.03	1.35	1.08	1.42	1.08	1.42	1.08	1.42	1.08	1.42	1.08	1.42	1.08	1.42	1.08	1.42	1.08	1.42	1.08	1.42	1.08	1.42	1.08	1.42	1.08	1.42
ZnO	0.93	0.91	1.08	1.12	1.35	1.31	0.80	0.82	0.77	0.83	0.86	0.86	0.86	0.86	0.86	0.86	0.86	0.86	0.86	0.86	0.86	0.86	0.86	0.86	0.86	0.86	0.86	0.86	0.86	0.86	0.86
SO ₄ ²⁻	46.38	46.38	46.38	46.38	46.38	46.38	46.38	46.38	46.38	46.38	46.38	46.38	46.38	46.38	46.38	46.38	46.38	46.38	46.38	46.38	46.38	46.38	46.38	46.38	46.38	46.38	46.38	46.38	46.38	46.38	46.38
NO ₃ ⁻	46.38	46.38	46.38	46.38	46.38	46.38	46.38	46.38	46.38	46.38	46.38	46.38	46.38	46.38	46.38	46.38	46.38	46.38	46.38	46.38	46.38	46.38	46.38	46.38	46.38	46.38	46.38	46.38	46.38	46.38	46.38
PM ₁₀	46.38	46.38	46.38	46.38	46.38	46.38	46.38	46.38	46.38	46.38	46.38	46.38	46.38	46.38	46.38	46.38	46.38	46.38	46.38	46.38	46.38	46.38	46.38	46.38	46.38	46.38	46.38	46.38	46.38	46.38	46.38

LOI = 100 × (M_{loss} / M_{dry})^a × 1000
 M_{loss} = 100 × (M_{wet} - M_{dry}) / M_{wet} × 1000
 M_{dry} = 100 × (M_{wet} - M_{loss}) / M_{wet} × 1000



448

449

450

451

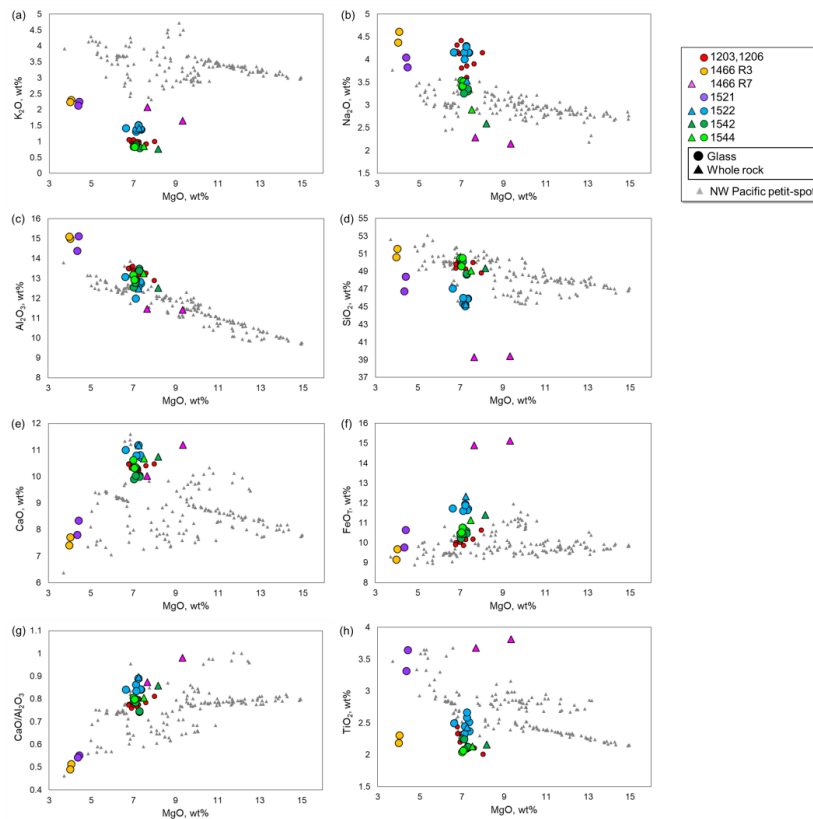
452

453

454

455

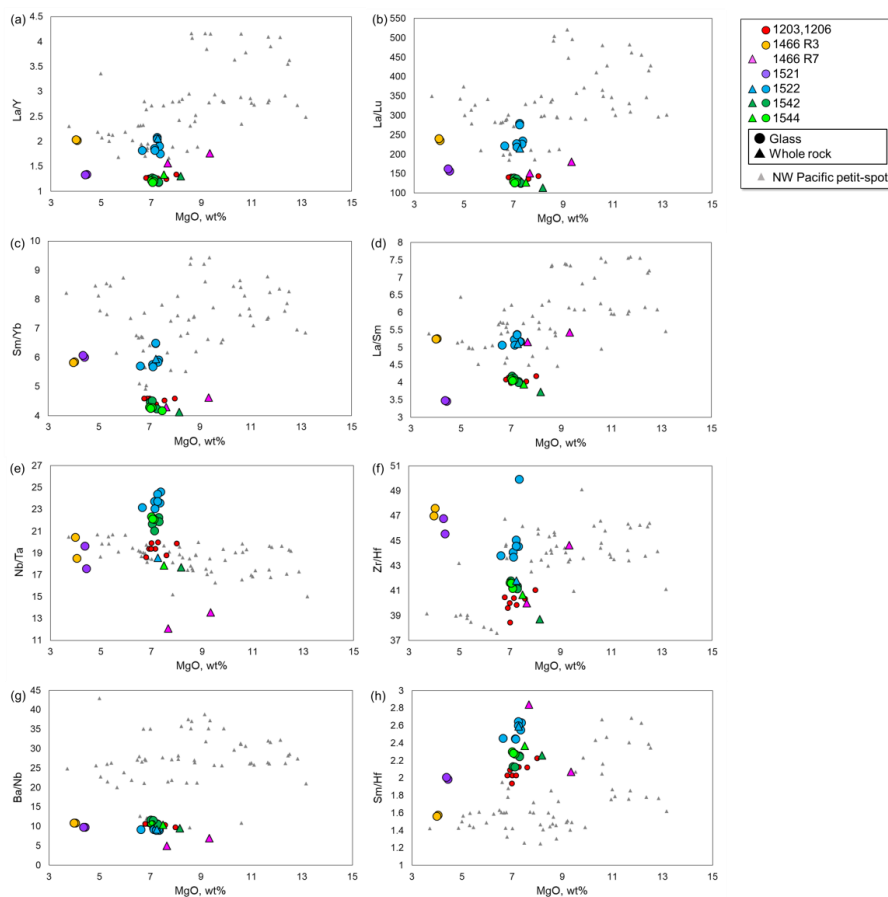
Fig. 4. Relationships between the SiO₂ and alkali contents. (a) Total alkali vs. silica diagram using the platform of Le Bas et al. (1986). The data are plotted as the total 100 wt%. The triangles and circles show the whole-rock and quenched-glass compositions, respectively. The compositions of the NW Pacific petit-spot are represented by gray triangles (Hirano and Machida, 2022). (b) SiO₂ vs. K₂O/Na₂O diagram. The data of Kimberlite, OIB (Ocean Island Basalt), and MORB (Mid Ocean Ridge Basalt) compiled in (b) were obtained from PetDB (<https://search.earthchem.org/>).



456



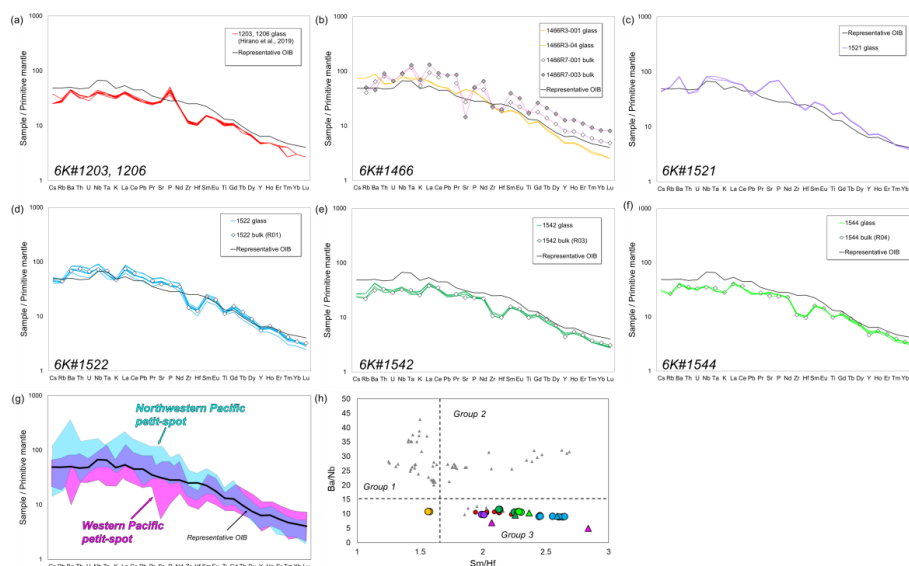
457 Fig. 5. Selected major-element oxides against MgO. The symbols correspond to those in Fig. 3.



458

459 Fig. 6. Selected trace-element ratios against MgO. The symbols correspond to those in Fig. 3.

460



461

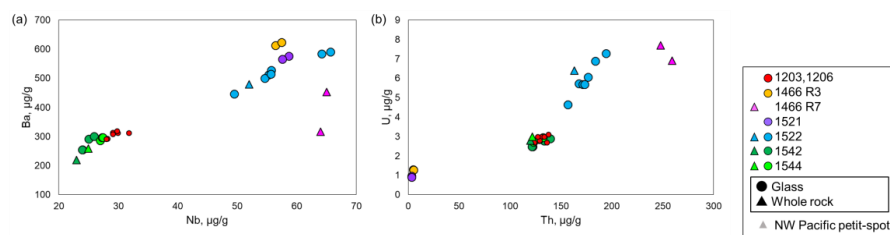
462 Fig. 7. Primitive mantle (PM)-normalized trace-element patterns (a)–(g) and element ratios (h). (g) The compositional

463 range of the study samples and NW Pacific petit-spots. (h) The Ba/Nb and Sm/Hf ratios of the petit-spot

464 basalts to discriminate the three groups after Machida et al. (2015). The symbols correspond to those in

465 Fig. 3. The PM composition was based on a study by Sun and McDonough (1989).

466



467

468 Fig. 8. Alteration sensitive elements (Ba and U) vs. insensitive elements (Nb and Th). The symbols correspond to

469 those in Fig. 3.

470

471

472 5.2 Sr–Nd–Pb isotopic composition

473

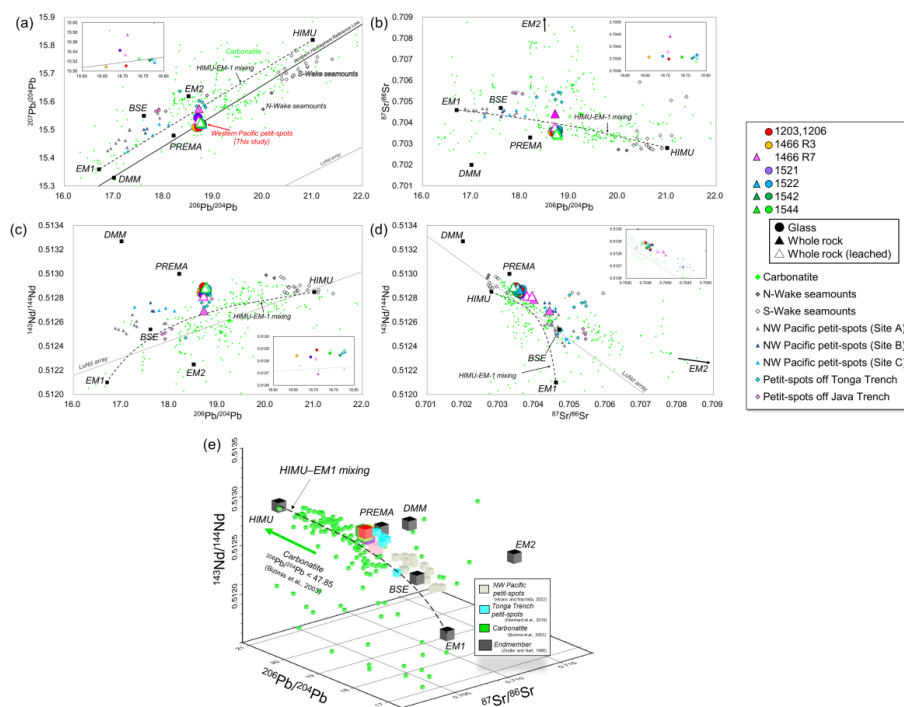
474 The Sr, Nd, and Pb isotopic compositions of the leached, unleached whole rock, and fresh glasses

475 in this study (presented in Table 3) were in practically identical ranges of $^{87}\text{Sr}/^{86}\text{Sr}$ (0.703412–

476 0.704424), $^{143}\text{Nd}/^{144}\text{Nd}$ (0.512694–0.512890), $^{206}\text{Pb}/^{204}\text{Pb}$ (18.6582–18.7778), $^{207}\text{Pb}/^{204}\text{Pb}$ (15.5086–



477 15.5749), and $^{208}\text{Pb}/^{204}\text{Pb}$ (38.6506–38.8041) despite their different locations (Figs. 9a–d, Table 3).
 478 The isotopic compositions of the quenched glass and whole rock were identical, indicating that the
 479 characteristics of the melting source could be obtained through the geochemistry of the young and
 480 fresh volcanic quenched glass. The leached and unleached materials of the same sample also had
 481 similar isotopic ratios, except for the 1466R7-003 basalt, which had a relatively high loss on ignition
 482 (LOI) (6.29 wt%) (Figs. 9a–d). The Sr–Nd–Pb isotopic three-dimensional (3D) plot is shown in Fig.
 483 9e.
 484



485
 486 Fig. 9. Sr–Nd–Pb isotopic variations of the petit-spot basalts. The mantle endmembers were derived from a study by
 487 Zindler and Hart (1986). The open triangles in (a)–(d) represent the acid-leached samples. Carbonatite
 488 data were compiled from GEOROC (<https://georoc.eu/georoc/new-start.asp>) with Bizimis et al. (2003).
 489 The northwestern (NW) Pacific petit-spots and petit-spots off the Tonga Trench were from Hirano and
 490 Machida (2022) and Reinhard et al. (2019), respectively. The petit-spots off the Java trench were from
 491 Taneja et al. (2016) and Falloon et al. (2022). The data of the Wake seamounts were from studies by
 492 Kononov and Martynov (1992), Koppers et al. (2003), Konter et al. (2008), Natland (1976), Smith et al.
 493 (1989), and Staudigel et al. (1991). The northern hemisphere reference line (NHRL) and Low Nd (LoNd)
 494 arrays were from studies by Hart (1984) and Hart et al. (1986), respectively. (e) The three-dimensional



495 (3D) plot of the Sr–Nd–Pb isotopic compositions. The compilation and mantle endmembers correspond to
 496 (a)–(d). The color usages of the plots were the same as (a)–(d). The mixing line between HIMU and EM-1
 497 is described as the following equation:

$$R_m = \frac{R_a f y + R_b (1-y)(1-f)}{R_a f y + R_b (1-y)(1-f)}$$

498 where R_a , R_b , and R_m are the isotopic ratios of component a, component b, and the mixture,
 499 respectively. f is a mixing ratio, and y is the ratio of concentration $\left(\frac{C_a}{C_a + C_b}\right)$.

501

Table 3
 Sr, Nd, and Pb isotopic compositions of western Pacific petit-spot basalts and measured standards.

Cruise	Sample name	Sample type	$^{87}\text{Sr}/^{86}\text{Sr}$	$^{142}\text{Nd}/^{144}\text{Nd}$	$^{206}\text{Pb}/^{204}\text{Pb}$	$^{207}\text{Pb}/^{204}\text{Pb}$	$^{208}\text{Pb}/^{204}\text{Pb}$
YK16-01	6K#1466 R3-004	Glass	0.703568 (06)	0.512842 (05)	18.6582 (07)	15.5086 (06)	38.6506 (19)
YK16-01	6K#1466 R7-001	Whole rock leached	0.703790 (05)	0.512817 (07)	18.7054 (20)	15.5337 (20)	38.8041 (50)
YK16-01	6K#1466 R7-001	Whole rock unleached	0.703989 (05)	0.512790 (06)			
YK16-01	6K#1466 R7-003	Whole rock leached	0.703933 (11)	0.512815 (05)			
YK16-01	6K#1466 R7-003	Whole rock unleached	0.704424 (05)	0.512694 (05)	18.7107 (06)	15.5749 (06)	38.7618 (17)
YK18-08	6K#1521 R04	Glass	0.703605 (05)	0.512832 (04)	18.6924 (06)	15.5428 (06)	38.7005 (19)
YK18-08	6K#1522 R01	Whole rock leached	0.703544 (05)	0.512881 (06)	18.7778 (09)	15.5209 (08)	38.7991 (22)
YK18-08	6K#1522 R01	Whole rock unleached	0.703590 (05)	0.512866 (06)	18.7705 (07)	15.5248 (07)	38.7905 (22)
YK18-08	6K#1522 R01	Glass	0.703656 (06)	0.512872 (04)	18.7773 (08)	15.5178 (07)	38.7904 (21)
YK19-05S	6K#1542 R03	Whole rock leached	0.703412 (07)	0.512890 (06)	18.7759 (10)	15.5244 (11)	38.7574 (36)
YK19-05S	6K#1542 R05	Glass	0.703517 (06)	0.512847 (04)	18.7653 (08)	15.5224 (07)	38.7345 (19)
YK19-05S	6K#1544 R04	Whole rock leached	0.703480 (04)	0.512883 (05)	18.7413 (14)	15.5262 (14)	38.745 (41)
YK19-05S	6K#1544 R04	Glass	0.703568 (05)	0.512863 (04)	18.7400 (08)	15.5253 (09)	38.7347 (22)
YK10-05	6K#1206 R04	Glass	0.703492 (05)	0.512890 (04)	18.7074 (06)	15.5109 (07)	38.6970 (19)
YK10-05	6K#1206 R04 duplicate	Glass			18.7071 (07)	15.5119 (07)	38.6950 (18)
Type of value	Standard for each isotope		$^{87}\text{Sr}/^{86}\text{Sr}$	$^{142}\text{Nd}/^{144}\text{Nd}$	$^{206}\text{Pb}/^{204}\text{Pb}$	$^{207}\text{Pb}/^{204}\text{Pb}$	$^{208}\text{Pb}/^{204}\text{Pb}$
Analyzed value	JB-2		0.703721 (05)	0.513094 (04)	18.3326 (05)	15.5453 (06)	38.2240 (17)
Reference value	JB-2 Sr, Nd: Onihashi et al. (1998), Pb: Tanimizu and Ishikawa (2006)		0.703709 (29)	0.513085 (08)	18.3315 (25)	15.5460 (21)	38.2240 (55)
Analyzed value	JNdi-1 (n=2)			0.512103 (05)			
Reference value	JNdi-1 Wakaki et al. (2007)			0.512101 (11)			
Analyzed value	SRM987 (n=2)		0.710239 (05)				
Reference value	SRM987 Weis et al. (2006)		0.710254 (02)				
Analyzed value	SRM981				16.9303 (05)	15.4828 (06)	36.6710 (16)
Reference value	SRM981 Tanimizu and Ishikawa (2006)				16.9308 (10)	15.4839 (11)	36.6743 (30)

Errors shown in parentheses represent 2σ and apply to the last two digits.

502

503

504 5.3 Age determination and estimation

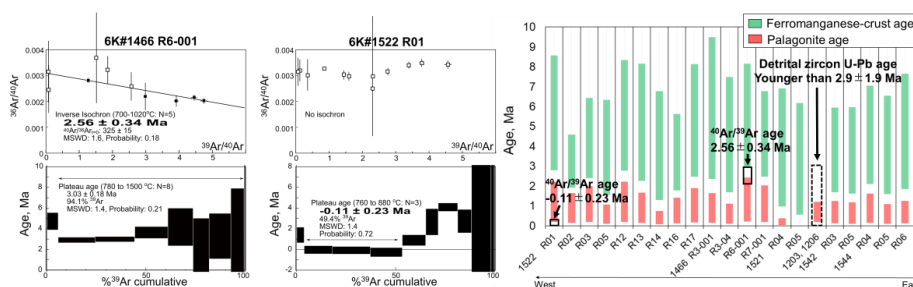
505

506 The $^{40}\text{Ar}/^{39}\text{Ar}$ ages were determined for two samples (1466R6-001 and 1522R01) (Fig. 10a,
 507 Table S2). Sample 1466R6-001 had a plateau age of 3.03 ± 0.18 Ma in seven fractions comprising
 508 94.1% released ^{39}Ar . However, the plateau age was recognized as apparently old, owing to excess ^{40}Ar ,
 509 as indicated by the initial $^{40}\text{Ar}/^{36}\text{Ar}$ ratio of 325 ± 15 , which exceeded the atmospheric ratio (296.0;
 510 Nier, 1950) in the inverse isochron. The inverse isochron age of 2.56 ± 0.34 Ma showed the best age
 511 estimate for the 1466R6-001 basalt (Fig. 10a). The 1522R01 sample released almost no radiogenic
 512 daughter nuclide (^{40}Ar in the K–Ar age system), and an age of -0.11 ± 0.23 Ma was gained in three
 513 fractions comprising 49% of the total released ^{39}Ar (Fig. 10a).

514 The ranges of eruption age were estimated for all the samples using the average thickness (n =
 515 20) of ferromanganese crust and palagonite rind (hydrated quenched glass) with their
 516 deposition/formation rates on the seafloor (ferromanganese crust, 1–10 mm/Myr; Hein et al., 1999;



517 palagonite, 0.03–0.3 mm/Myr; Moore et al., 1985) (Fig. 10b). Using this approach, the western Pacific
 518 petit-spots were expected to have erupted later than ca. 9 Ma. The ranges of eruption age estimated
 519 from palagonite rind did not overlap with those from ferromanganese crust showing older durations,
 520 although they had general correlations (Fig. 10b). The $^{40}\text{Ar}/^{39}\text{Ar}$ ages of two samples and the detrital
 521 zircon age of the 1203 and 1206 samples (Hirano et al., 2019) were overlaid within these ranges.
 522



523

524 Fig. 10. Geochronological data. (a) The $^{40}\text{Ar}/^{39}\text{Ar}$ ages of the 6K#1466R6-001 and 6K#1522R01 basalts. The errors
 525 show a 2-sigma confidence level. (b) Estimated relative ages using the thickness of ferromanganese crust
 526 (green bands) and palagonite (hydrated quenched-glass rind; red bands) covered with petit-spot basalts.
 527 These values were estimated using the average for each sample ($n = 20$).

528

529 6 Discussion

530

531 6.1 Eruptive setting of western Pacific petit-spots

532

533 Here, two crystalline petit-spot basalts were successfully subjected to $^{40}\text{Ar}/^{39}\text{Ar}$ dating. A
 534 previously reported petit-spot knoll in this region (examined during the 6K#1203 and 1206 dives) aged
 535 “younger than 3 Ma” was investigated using the U–Pb dating of eight detrital zircons in peperites (Fig.
 536 10b) (Hirano et al., 2019). The results showed that the silica-undersaturated vesicular basalt of
 537 6K#1466R6-001, as a host of ultramafic xenoliths (Mikuni et al., 2022), exhibited a $^{40}\text{Ar}/^{39}\text{Ar}$ age of
 538 2.56 ± 0.34 Ma (Fig. 10). Oppositely, the fresh vesicular basalt of 6K#1522R01, which erupted at the
 539 foot of the 100-Ma Takuyo-Daigo seamount (Fig. 2) (Nozaki et al., 2016), did not exhibit radiogenic
 540 ^{40}Ar highlighting that this sample is quite young (approximately 0 Ma) (Fig. 10). The ranges of
 541 eruption ages were estimated using the average thickness of ferromanganese crust and palagonite rind
 542 (seawater-hydrated quenched glass) with their deposition/formation rates on the seafloor. The
 543 $^{40}\text{Ar}/^{39}\text{Ar}$ and zircon U–Pb ages were within these ranges (Fig. 10). Here, the petit-spot volcanic field
 544 was surrounded by Cretaceous seamounts (Koppers et al., 2003) and irregular Paleogene volcanoes
 545 (Aftabuzzaman et al., 2021; Hirano et al., 2021). However, no zero-aged hotspots were observed in



546 this region, and the P-wave tomographic image of the surface to the core–mantle boundary of the study
547 area did not exhibit a plume-like low-velocity zone (Fig. 1c; Lu et al., 2019). Furthermore, the MORB-
548 like to more depleted noble-gas isotopic compositions of the petit-spot knoll (6K#1203, 1206)
549 suggested its upper mantle origin (Yamamoto et al., 2018). Along with the outer-rise bulge in front of
550 the Mariana Trench detected through a positive gravitational anomaly (Hirano et al., 2019), these data
551 suggested that the western Pacific petit-spot volcanoes could have erupted at ~0–3 Ma owing to the
552 flexure of the subducting Pacific Plate into the Mariana and Ogasawara Trenches.

553 The petit-spot basalts from the 6K#1542 and 1544 dives could have originated from the same
554 eruptive source based on their similar petrographic and geochemical features despite a distance of
555 approximately 6.8 km between both (Figs. 3d, 4, 5, 6, 7, 8, and 9). Contrarily, in terms of their
556 petrographies and geochemistries, the basalts from the 6K#1466 dive were discriminated between the
557 samples from the lava flows on the abyssal plain (R3-001 and R3-004) and the samples from the knoll
558 site (R6-001, R7-001, and R7-003). The R3 basalts were collected at a lava outcrop 600 m south of
559 the knoll, and the R6 and R7 samples were collected on the western slope of the knoll (Fig. 3a). The
560 6K#1466R3 series were glassy with a high SiO₂ content (50.6–51.6 wt%), including minor plagioclase
561 and less vesicles (Figs. 3a and 4a). However, the 6K#1466R6 and R7 series exhibited silica-
562 undersaturated compositions (SiO₂ = 39.3–39.4 wt%) and high vesicularities (20–40 vol.%) (Figs. 3b
563 and 4a). Combining these observations with the differences in MgO contents and trace element
564 compositions, the R3 and R6–R7 basalts were suggested to have different parental magmas (Figs. 6
565 and 7b). Generally, vesicular samples (6K#1203, 1206, 1466R7, 1522, 1542, and 1544 basalts) were
566 relatively primary (i.e., MgO > 6.63 wt%), whereas nonvesicular samples (6K#1466R7 and 1521
567 basalts) were evolved (i.e., MgO < 4.43 wt%). This correlates with the compositions of olivine
568 microphenocrysts in the low forsterite content ($Fo\# = 100 \times \text{Mg}/[\text{Mg} + \text{Fe}^{2+}]_{\text{cation}}$) of olivine in evolved
569 basalts and the high Fo# of olivine in the relatively primary basalts (Figs. S1a–c).

570 The CI chondrite-normalized REE ratios of this study samples were within those of OIBs, and
571 the REE patterns revealed HREE-depleted patterns (Fig. S3). However, among the western Pacific
572 petit-spots, the REE and trace element ratios differed for each volcano (i.e., parental magmas) (Figs.
573 6 and S3). Given the lack of correlation between MgO and the trace element ratios, each volcano could
574 have originated from isolated sources (i.e., melt ponds) with different chemical compositions and
575 degrees of melting (Fig. 6). Oppositely, the radiogenic Sr, Nd, and Pb isotopic ratios of the samples
576 were nearly identical, and the components in the source were probably equivalent (Fig. 9).

577 Summarily, (1) the western Pacific petit-spot volcanoes erupted at ~0–3 Ma owing to the plate
578 flexure related to the subduction of the Pacific Plate into the Mariana Trench (Figs. 1 and 2). (2) The
579 6K#1542 and 1544 samples originated during the same magmatic event (Fig. 3d). However, the basalts
580 from the 6K#1466 dive were subdivided into two parental magmas (R3 and R6–R7 basalts) (Fig. 3a).
581 (3) Each volcano originated from isolated source and/or ascending processes based on the independent



582 trace element ratios. The geochemical components involved in the source, however, were similar
583 among the western Pacific petit-spot volcanoes because of the nearly identical Sr, Nd, and Pb isotopic
584 compositions (Figs. 6 and 9). A variation in the trace element compositions among the volcanoes was
585 plausibly due to the degree of contribution of carbonatite flux and/or the recycled crustal component
586 to the source, as discussed below.

587

588 **6.2 Petit-spot magma composition and its evaluation**

589

590 Post-eruption seawater alteration might affect the chemical composition of oceanic basalts. Thus,
591 various approaches, including petrographic observation, geochemical investigation, and acid leaching,
592 have been employed to evaluate the primary features and the removal of this effect for isotopic analysis
593 (Hanano et al., 2009; Melson et al., 1968; Miyashiro et al., 1971; Nobre Silva et al., 2009; Resing and
594 Sansone, 1999; Staudigel and Hart, 1983; Zakharov et al., 2021). The study samples exhibited whole-
595 rock LOI in the range of 0.67–1.72 wt%, excluding two relatively altered samples, 6K#1466R7-001
596 (LOI = 2.68 wt%) and R7-003 (LOI = 6.29 wt%). The lack of secondary phases (e.g., clay minerals)
597 implied that the seawater alteration of petit-spot basalts was limited. The present petit-spot basalts
598 generally comprised fresh olivine, clinopyroxene, glass, and certain minor phases. These features
599 corresponded to the petrography of typical monogenetic alkaline basaltic volcanoes (Brenna et al.,
600 2021). Pristine quenched glasses were preserved in most of the samples, excluding three exceptional
601 samples (the 6K#1466R6-001, R7-001, and R7-003 basalts). Positive correlations were observed
602 between the alteration-insensitive (e.g., Nb, Th) and -sensitive (e.g., Ba, U) incompatible elements.
603 This indicated that the effect of seawater alteration was not extensive, excluding the 6K#1466R7-001
604 and R7-003 basalts (Fig. 8). Although each sample was derived from different volcanic edifices, the
605 positive correlation of all the study samples was due to the chemical similarity of the source
606 compositions for certain elements (i.e., Ba/Nb and U/Th ratios were nearly constant among the
607 samples), as well as the Sr, Nd, and Pb isotopic compositions (Fig. 9). These observations showed that
608 practically all the petit-spot basalts were unaffected by seawater alteration.

609 The variable MgO (4–9 wt%), Ni (<263 ppm), and Cr (<350 ppm) contents in the samples were
610 lower than the expected values of primary mantle-derived melt (MgO >10 wt%, Ni >400 ppm, Cr
611 >1000 ppm; Frey et al., 1978). Similarly, the Mg# ($100 \times \text{Mg}/[\text{Fe}^{2+} + \text{Mg}]_{\text{molar}}$) values were
612 differentiated in the range of 41–57 (Table 2) against the primary basaltic melt, which was equilibrated
613 with the upper mantle (Mg# = 66–75; Irving and Green, 1976). No phenocrysts were discovered (i.e.,
614 only microphenocryst were observed), despite such differentiated compositions as well as most of the
615 NW Pacific petit-spot basalts. This suggested that the western Pacific petit-spots experienced magma-
616 stagnation and crystal fractionation in the lithosphere as well (Machida et al., 2017; Valentine and
617 Hirano, 2010; Hirano, 2011; Yamamoto et al., 2014). The mass balance calculation of the fractional



618 phases of the petit-spot basalts using the mineral modal composition could not be performed because
619 of inadequate phenocrysts. However, the trends of the major elements of the samples implied the
620 crystal fractionation of the same phases. The negative trends of the Al_2O_3 content and the positive
621 trends of the CaO and CaO/ Al_2O_3 content with a decrease in MgO indicated the occurrence of olivine,
622 spinel, and clinopyroxene fractionation (Figs. 5c, e, and g). The absence of visible correlations of the
623 K_2O , Na_2O , SiO_2 , and TiO_2 contents against MgO suggested that the fractionation of plagioclase and
624 the Fe–Ti oxides was insignificant. The Fe–Ti oxides as minor phases in the groundmasses and
625 plagioclases were only observed in the most differentiated 1466R3-001 and R3-004 basalts (Figs. 3,
626 5a, b, d, and h). However, these major elemental trends should be interpreted as apparent trends
627 because each petit-spot volcano originated from an isolated parental magma with different chemical
628 composition or degree of partial melting as discussed above.

629 The trace element composition of alkali basalts can be used to determine the melting source
630 rather than major elements (Hofmann, 2003; Machida et al., 2014, 2015). Trace element composition
631 of magma, however, could be modified by crustal and/or mantle assimilation and fractionation of
632 certain minerals. The relatively primitive basalts (6K#1203, 1206, 1466R6, R7, 1522, 1542, and 1544)
633 included xenocrystic olivines and partly ultramafic xenoliths, indicating a rapid magma ascent (Hirano
634 et al., 2019; Mikuni et al., 2022; Fig. S4). However, since the stagnation of ascending petit-spot magma
635 could occur to create fertile peridotite and pyroxene-rich veins from the middle to lower depths of the
636 lithosphere (Mikuni et al., 2022; Pilet et al., 2016), the chemical composition of the petit-spot magma
637 could be modified because of assimilation with the ambient lithospheric peridotite. According to
638 Hirano and Machida (2022), ascending silica-undersaturated melt would mainly consume
639 orthopyroxene (\pm spinel) and become a more silicic composition with Zr and Hf depletion. This is
640 because of the relatively higher Zr–Hf partition of orthopyroxene than those of other trace elements
641 (Pilet et al., 2008; Shaw, 1999; Tamura et al., 2019). The orthopyroxenes of fertile pyroxenites and
642 lherzolite xenoliths metasomatized by petit-spot melts exhibited Zr and Hf enrichment (Mikuni et al.,
643 2022; Fig. S5). If this silica-enrichment (i.e., melt–rock interaction) was significant, a positive
644 correlation between SiO_2 and Sm/Hf was expected as a mantle assimilation trend. However, the
645 samples exhibited a negative correlation, similar to those of the NW Pacific petit-spots (Hirano and
646 Machida, 2022) (Fig. S2). Considering the relationship between the Sm and Hf partition coefficients
647 of clinopyroxene (i.e., $D^{\text{Hf}} < D^{\text{Sm}}$; McKenzie and O’Nions, 1991; Kelemen et al., 2003), we suggest
648 that the negative correlation between the Sm/Hf and SiO_2 of the petit-spot basalts probably reflected
649 the crystal fractionation of clinopyroxene rather than mantle assimilation. The Ba/Nb ratios of the
650 samples were nearly constant and did not correlate with the MgO and SiO_2 contents (Figs. 6g and S2g).
651 The lack of correlation between the other trace element ratios, excluding Sm/Hf and Ba/Nb (i.e., La/Y,
652 La/Lu, Sm/Yb, La/Sm, Nb/Ta, Zr/Hf), and the MgO concentration implied that crystal fractionation
653 may not have been involved with those of the incipient melt (Fig. 6). However, it is difficult to



654 independently follow the evolution of the trace element composition for each volcano since each
655 volcano originated from isolated sources. Thus, considering the observations above, the fresh and zero-
656 aged 6K#1522 basalts (the highest Sm/Hf ratios and lowest SiO₂ contents among the fresh samples
657 and higher MgO contents) were selected for further analysis with geochemical modeling. Considering
658 that the 6K#1522 samples had MgO in the range of 6.63–7.36 wt%, olivine was expectedly the
659 dominant phase of crystal fractionation (Asimow and Langmuir, 2003; Helz and Thornber, 1987;
660 Herzberg, 2006). When the olivine maximum fractionation model (Takahashi et al., 1986; Tatsumi et
661 al., 1983) was applied to test two samples, the calculated primary trace element contents did not
662 significantly differ from those of the analytical compositions (Table S3 and Fig. S6). Thus, the
663 6K#1522 basalts were assumed to be the most primary petit-spot basalt samples and were used to
664 evaluate the geochemical modeling results.

665

666 **6.3 Melting source of western Pacific petit-spots**

667

668 Petit-spot magma is considered to originate from the asthenospheric mantle based on MORB-
669 like noble gas isotopic compositions and a multiphase saturation experiment (Hirano et al., 2006, 2013;
670 Machida et al., 2015, 2017; Yamamoto et al., 2018, 2020). The depletions of specific elements (e.g.,
671 U, Th, Nb, Ta, Zr, Hf, and Ti) of petit-spot basalts potentially demonstrate the involvement of
672 carbonatitic materials in conjunction with a large amount of CO₂ and lower Mg isotopic ratio than that
673 of the normal mantle (Dasgupta et al., 2009; Hirano and Machida, 2022; Liu et al., 2020; Okumura
674 and Hirano, 2013). Other oceanic lavas originating from the asthenosphere (e.g., Hawaiian rejuvenated
675 lavas and North Arch volcanoes) exhibited characteristic trace element signatures (i.e., Zr and Hf
676 depletion) similar to those of petit-spot lavas. This implied that their melting sources were involved
677 with carbonatitic materials with or without plume-derived components (Fig. S7; Borisova and Tilhac,
678 2021; Clague and Frey, 1982; Clague et al., 1990; Dixon et al., 2008; Yang et al., 2003). In addition,
679 the involvement of recycled crustal components was inferred from the geochemical features of the
680 petit-spot basalts, and the upper mantle was revealed to be heterogeneous (Liu et al., 2020; Machida
681 et al., 2009, 2015). Such a scenario of the source on petit-spot magma was consistent with the
682 previously suggested petrogenesis of alkaline rocks explained by the addition of CO₂-rich components
683 and/or recycled crustal materials with or without sediment to the mantle (e.g., Dasgupta et al. 2007;
684 Hoffmann, 1997). Conversely, the melting of an amphibole-rich metasomatic vein explains the major
685 and trace element composition of alkali basalts (Pilet et al., 2008; Pilet, 2015). However, the
686 experimentally produced melts exhibited Pb depletion and a positive Nb-Ti anomaly in the PM-
687 normalized trace element patterns (Fig. S8) inconsistent with the petit-spot basalts (Fig. 7). In addition,
688 Juriček and Keppler (2023) demonstrated that amphibole dehydration is not the cause for the oceanic
689 LAB by high-pressure experiment on the realistic condition. The fertile pyroxenitic xenoliths and



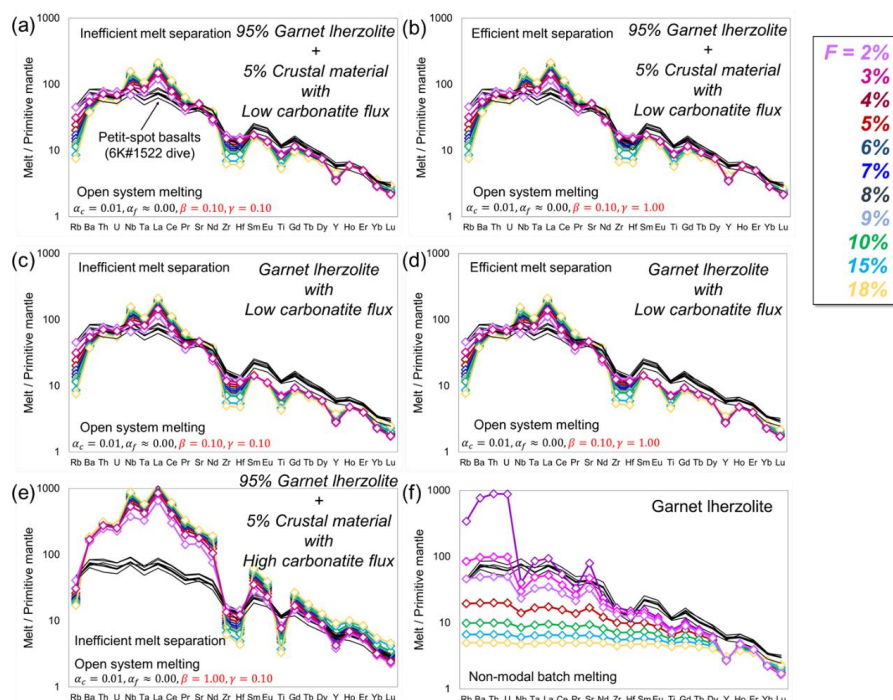
690 pyroxene xenocrysts occurring in the 1466R6 and R7 basalts, which originated from the metasomatic
691 vein related to prior petit-spot magmatism, had neither amphiboles nor other hydrous minerals (Mikuni
692 et al., 2022).

693 To discuss the involvement of carbonatitic and crustal components in petit-spot melts, a partial
694 melting model of the heterogeneous mantle was provided. The involvement of carbonatitic fluids and
695 recycled materials in the genesis of petit-spot melts was suggested, and the open-system model with
696 carbonatite influx from the outer system was employed using “OSM-4” of Ozawa (2001). The
697 parameters are listed in Table S4, and the details are described in Sect. 4.4. As a result, the low
698 carbonatite-influx melting ($\beta = 0.1$) of garnet lherzolite with a small amount (5%) of the crustal
699 component was the most plausible model of petit-spot magma generation (Figs. 11a and b). The results
700 also showed that the melt-separation ratio was insignificant to the trace element composition of the
701 calculated melts (Figs. 11a and b). The partial melting of garnet lherzolite with carbonatite influx
702 without crustal components exhibited small offsets of Sm to Lu from the petit-spot basalts in the trace
703 element patterns (Figs. 11c, d). The high carbonatite influx could not explain the trace element
704 composition of the petit-spot basalts (Fig. 11e). Moreover, the modeled partial melting of garnet
705 lherzolite by non-modal batch melting (Shaw, 1970) was inconsistent with the petit-spot patterns (Fig.
706 11f). Thereafter, we concluded that the partial melting of garnet lherzolite with low carbonatite flux
707 and small crustal components plausibly explained the source of petit-spot volcanoes (Figs. 11a and b).
708 Assuming that the trace element composition of 6K#1203, 1206, 1542, and 1544 basalts were also
709 primitive, they may be explained by a partial melting of garnet lherzolite with 5% crustal component
710 and lower carbonatite influx rate ($\beta = 0.03$) (Fig. S9). Actually, the 6K#1203, 1206, 1542, and 1544
711 basalts exhibited the similar MgO contents and Mg# to those of 6K#1522 basalts (Fig. 4 and Table 2).
712 These result provides quantitative evidence on the petrogenesis of petit-spots and asthenospheric
713 magmas with similar trace element compositions, i.e., the contribution of carbonatite melt and recycled
714 oceanic crust.

715 Although the melting source contained small proportions of carbonatite melt and crustal
716 components, these components could have contributed to the isotopic composition because of their
717 abundant incompatible elements rather than the ambient mantle. The determination of the Sr, Nd, and
718 Pb isotopic compositions revealed that they had geochemically identical prevalent mantle (PREMA)-
719 like sources. They did not belong to any mantle isotopic endmembers (i.e., depleted MORB mantle
720 (DMM); EM-1, -2; and HIMU; Fig. 9) contrary to those of NW Pacific petit-spots toward the EM-1
721 isotopic composition (Machida et al., 2009; Liu et al., 2020). In the Pb isotopic space, the present
722 samples did not correlate with those of the neighboring HIMU-like Cretaceous seamounts (Fig. 9a)
723 (N-Wake, S-Wake seamounts; Konter et al., 2008; Koppers et al., 2003; Natland, 1976; Smith et al.,
724 1989; Staudigel et al., 1991). For the melting source of the NW Pacific petit-spot basalts, the
725 contributions of the eclogite/pyroxenite endmember as recycled oceanic crust and the carbonated



726 endmember were suggested based on the major and trace elements and the Mg, Sr, Nd, and Pb isotopic
727 compositions with the Mg diffusion modeling (Liu et al., 2020). The higher FeO/MnO ratios of the
728 present melts (65.9–78.0), compared with those of partial melts originating from peridotite (50–60),
729 were attributed to the presence of recycled pyroxenite (Herzberg, 2011). This could have contributed
730 to the crustal components in the melting source. However, the western Pacific petit-spots in this study
731 identically exhibited a PREMA-like isotopic signature without extreme endmember contributions (Fig.
732 9). Such isotopic compositions with the world's petit-spots can be possibly explained by the diverse
733 mixing proportion of HIMU and EM-1 components (Fig. 9e). The the isotopic compositions of the
734 NW Pacific petit-spots (off the Japan Trench), Samoan petit-spots (off the Tonga Trench), petit-spot
735 dikes in Christmas Island (off the Java trench), and western Pacific petit-spots (off the Mariana Trench
736 in this study) were roughly along the HIMU–EM-1 mixing line (Fig. 9e). Furthermore, the isotopic
737 compositions of global carbonatites can be generally explained by the mixing of HIMU and EM-1
738 (Bell and Tilton, 2002; Hoernle et al., 2002; Hulett et al., 2016). The contributions of the carbonated
739 material/carbonatite and crustal components to the melting source were suggested in terms of the
740 origin of HIMU and EM-1 (Collerson et al., 2010; Hanyu et al., 2011; Wang et al., 2018; Weiss et al.,
741 2016; Workman et al., 2004; Zindler and Hart, 1986). Although the HIMU and EM-1 components
742 could not be determined to be carbonatite and recycled crust, respectively, owing to the various views
743 on each tectonic setting for the mantle endmember, the isotopic signatures may suggest the
744 involvement of carbonatitic and recycled crustal materials. The mass balance models on the trace
745 elements and the isotopic variations in the petit-spot volcanoes confirmed the contribution of
746 carbonatite melt and the recycled oceanic crust to the melting source of the western Pacific petit-spots
747 (Fig. 12).



748

749

750

751

752

753

754

755

756

757

758

759

760

761

762

763

764

765

Fig. 11. Geochemical modeling for the primitive mantle (PM)-normalized trace-element pattern. The calculated hypothetical melts of 5% crustal component-bearing lherzolite with low ($\beta = 0.1$) carbonatite influx at an (a) inefficient melt-separation rate ($\gamma = 0.1$), and (b) efficient melt-separation rate ($\gamma = 1.0$) are shown. The same models without crustal components are also represented at an (c) inefficient melt-separation rate ($\gamma = 0.1$) and (d) efficient melt-separation rate ($\gamma = 1.0$). (e) The 5% crust-bearing lherzolite with high carbonatite-fluxing. (f) Non-modal batch melting of garnet lherzolite. F is the degree of melting (%). The trace-element composition of the western Pacific petit-spot basalts from the 6K#1522 dive is shown as black lines for comparison. The PM composition of lherzolite and the N-MORB composition of recycled crust were based on a study by Sun and McDonough (1989). The influx carbonatite is the “average carbonatite” of a study by Bizimis et al. (2003). The parameters used in the open-system melting models were as follows: α_c is a critical melt fraction, α_f is a final trapped melt fraction, β is a melt influx rate, and γ is a melt-separation rate. Detailed information is provided in Section 4-4 and Table S2.

6.4 Where does carbonatite originate from?

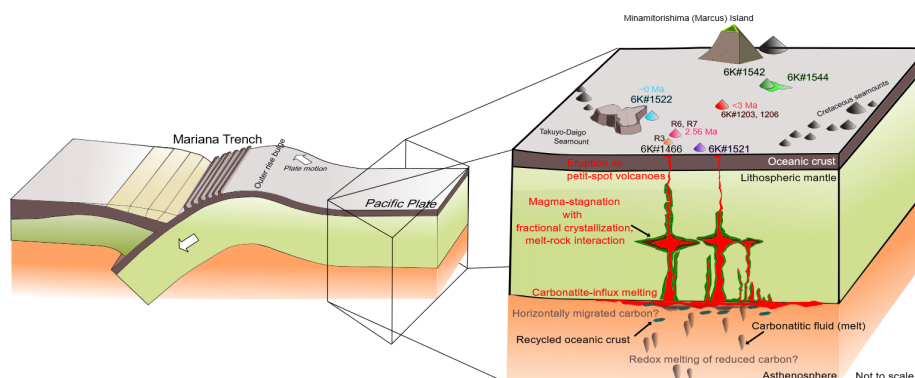
The origin of carbonatite is under debate and is ambiguous. The expected petrogenesis of



766 carbonatite is diverse, and a wide range of views exist on how carbonatite melt occurs in the deep
767 mantle (Carnevale et al., 2021). Natural carbonatites frequently used as reference values originate from
768 the Canary and Cape Verde hotspots in the Atlantic Ocean (Hoernle et al., 2002). Those used as average
769 values originate from the East African Rift, Canadian Craton, and South African Craton (i.e., average
770 carbonatite; Bizimis et al., 2003). The presence of such carbonatite magmas accounts for the carbon
771 cycle in the deep mantle. Previous studies on the direct measurement of deep-originated carbonatite
772 have focused on the carbonatite fluid inclusion in diamonds (Weiss et al., 2016) and the carbonate
773 globule observed in the post-spreading ridge basalt in the South China Sea (Zhang et al., 2017; Zhong
774 et al., 2021).

775 Experimental studies have revealed the various petrogenesis of carbonatite and carbonatitic
776 alkali-rich magma under high pressures (Dasgupta et al., 2006; Ghosh et al., 2009). Among their
777 interpretations, the conceivable origin of carbonatite possibly related to the occurrence of petit-spot
778 melt is subducted carbonated pelite, pyroxenite/eclogite, or peridotite stored as diamond or metal
779 carbide in the reduced lower portion of the upper mantle (Liu et al., 2020; Rohrbach et al., 2007).
780 Subducted carbonated pelite, for example, would melt under high pressure (>8 GPa) in a transition
781 oxidation state (i.e., redox melting; Grassi and Schmidt, 2011). Chen et al. (2022) demonstrated that
782 the alkali-rich carbonatite melt could occur under a pressure higher than 6 GPa, particularly exhibiting
783 K-rich and Na-rich carbonatites under 6–12 and >12 GPa, respectively. This pressure-dependent
784 alkalinity of the produced carbonatite melts might explain the variation between potassic NW Pacific
785 petit-spot lavas and present sodic petit-spot lavas (Fig. 4b). An experimental study pointed out the
786 existence of a carbonate-rich layer in the LAB owing to the horizontally spread carbonate from around
787 the wedge mantle rather than upwelling from the deep mantle (Hammouda et al., 2020). The small
788 degree of partial melt containing 5–6 wt% CO₂ at 3 GPa also explains the electrical conductivities of
789 the asthenosphere (Sifré et al., 2014). Although the multiple origins of carbonatite are merely
790 suggested and remain unconfirmed, carbon-rich components exist in the upper mantle and function as
791 melting agents of petit-spot magma, given the geochemical characteristics of petit-spot basalts.

792



793

794 Fig. 12. Schematic illustration of the magmatic processes of the western Pacific petit-spot volcanoes.

795 Carbonatitic melt and recycled oceanic crust potentially induce partial melting of asthenospheric mantle
 796 beneath the western Pacific region. Carbonatitic melt might have originated from a carbon-rich
 797 component horizontally migrated from a subduction zone (Hammouda et al., 2021), or a redox melting
 798 of reduced carbon in the deep mantle (Chen et al., 2022; Grassi and Schmidt, 2011; Rohrbach et al., 2007).
 799 Petit-spot magma stagnated in the lithosphere with fractional crystallization and melt-rock interaction
 800 (Mikuni et al., 2022), and they have erupted at ~0–3 Ma.

801

802

803 **7 Conclusion**

804

805 The occurrence of petit-spot volcanism supports partial melting at the LAB, providing crucial
 806 implications for the nature of this geophysical discontinuity. Multiple petit-spot magmatisms on the
 807 western Pacific Plate occurred at ~ 0–3 Ma, originating from similar PREMA-like melting sources
 808 based on $^{40}\text{Ar}/^{39}\text{Ar}$ dating and the Sr, Nd, and Pb isotopic compositions. The mass balance-based open-
 809 system modeling for trace elements revealed that the western Pacific petit-spot magma was generated
 810 by the partial melting of a small amount (5%) of oceanic crust-bearing garnet lherzolite with
 811 carbonatite influx. This correlated with the theory of previous studies on petit-spots and several
 812 experimental studies for the generation of LAB. The Sr, Nd, and Pb isotopic compositions of this study
 813 samples, with those of the NW Pacific petit-spots, off the Tonga and Java Trenches, could be explained
 814 by mixing the EM-1-like and HIMU-like components, which contribute to subducted
 815 carbonated/crustal materials. The tectonic-induced magmatism, like a petit-spot, may have the same
 816 melting mechanism.

817

818 **Authorship contributions**



819

820 K. Mikuni and N. Hirano conceived the project and performed all experiments. S. Machida and
821 Y. Kato contributed the Sr, Nd, and Pb isotopic analysis using TIMS and MC-ICP-MS. H. Sumino
822 contributed the $^{40}\text{Ar}/^{39}\text{Ar}$ dating. N. Akizawa, A. Tamura, and T. Morishita helped and performed
823 EPMA and LA-ICP-MS analyses. S. Machida and N. Hirano conducted the research cruises to gain
824 the rock samples. All authors interpreted the data and wrote the manuscript with comments and
825 improvements.

826

827 **Competing Interest**

828

829 The authors declare that they have no conflict of interest.

830

831 **Data availability**

832

833 The data newly analyzed in this study and results of geochemical modeling are included in
834 digital format in the online data repository of this paper (Tables 1, 2, and 3, and Supplementary Tables
835 S1 to S4) and the EarthChem online database (DOI will be obtained when it is accepted).

836

837 **Acknowledgement**

838

839 We would like to thank the captains, crews, and shipboard scientific parties of the R/V *Yokosuka*
840 and the operating team of the submersible *Shinkai 6500* for their great work during the YK16-01,
841 YK18-08, and YK19-05S cruises. The Kyoto University Research Reactor Institute is gratefully
842 acknowledged in their assistance of undertaking the radiometric dating. We would like to express our
843 great appreciation to Prof. T. Tsujimori (ORCID: 0000-0001-9202-7312) for his effort in management
844 of the laboratory at Tohoku University. We also thank R. Fukushima (ORCID: 0000-0003-2683-6757)
845 for improving the wording in the manuscript. We are really grateful Y. Matamura and Y. Jindo for their
846 help and discussion on scientific matters. The authors would like to thank Enago (www.enago.jp) for
847 the English language review. This research was supported by the Cooperative Program (No. 106, 202)
848 of Atmosphere and Ocean Research Institute, The University of Tokyo. The Japan Society for the
849 Promotion of Science (Grant Numbers 17K05715, 18H03733, 20K04098) also supported this research.

850

851 **References**

852

853 Aftabuzzaman, M.R., Yomogoda, K., Suzuki, S., Takayanagi, H., Ishigaki, A., Machida, S., Asahara,
854 Y., Yamamoto, K., Hirano, N., Sano, S.-I., Chiyonobu, S., Bassi, D. and Iryu, Y.: Multi-
855 approach characterization of shallow-water carbonates off Minamitorishima and their
856 depositional settings/history, *Island Arc*, 30, e12400, <https://doi.org/10.1111/iar.12400>, 2021.



- 857 Akizawa, N., Ozawa, K., Tamura, A., Michibayashi, K. and Arai, S.: Three-dimensional evolution of
858 melting, heat and melt transfer in ascending mantle beneath a fast-spreading ridge segment
859 constrained by trace elements in clinopyroxene from concordant dunites and host
860 harzburgites of the Oman ophiolite, *J. Petrol.*, *57*, 777–814,
861 <https://doi.org/10.1093/petrology/egw020>, 2016.
- 862 Akizawa, N., Ohara, Y., Okino, K., Ishizuka, O., Yamashita, H., Machida, S., Sanfilippo, A., Basch,
863 V., Snow, J.E., Sen, A., Hirauchi, K.-I., Michibayashi, K., Harigane, Y., Fujii, M., Asanuma,
864 H. and Hirata, T.: Geochemical characteristics of back-arc basin lower crust and upper
865 mantle at final spreading stage of Shikoku Basin: an example of Mado Megamullion, *Prog.*
866 *Earth Planet. Sci.*, *8*, 65, <https://doi.org/10.1186/s40645-021-00454-3>, 2021.
- 867 Akizawa, N., Hirano, N., Matsuzaki, K.M., Machida, S., Tamura, C., Kaneko, J., Iwano, H.,
868 Danhara, T. and Hirata, T.: A direct evidence for disturbance of whole sediment layer in the
869 subducting Pacific plate by petit-spot magma–water/sediment interaction, *Mar. Geol.*, *444*,
870 106712, <https://doi.org/10.1016/j.margeo.2021.106712>, 2022.
- 871 Asimow, P. D. and Langmuir, C. H.: The importance of water to oceanic mantle melting regimes,
872 *Nature*, *421*, 815–820, <https://doi.org/10.1038/nature01429>, 2003.
- 873 Audhkhasi, P. and Singh, S.C.: Discovery of distinct lithosphere-asthenosphere boundary and the
874 Gutenberg discontinuity in the Atlantic Ocean, *Sci. Adv.*, *8*, eabn5404,
875 <https://doi.org/10.1126/sciadv.abn5404>, 2022.
- 876 Axen G.J., van Wijk, J.W. and Currie, C.A.: Basal continental mantle lithosphere displaced by flat-
877 slab subduction, *Nat. Geosci.*, *11*, 961–964, <https://doi.org/10.1038/s41561-018-0263-9>,
878 2018.
- 879 Azami, K., Machida, S., Hirano, N., Nakamura, K., Yasukawa, K., Kogiso, T., Nakanishi, M. and
880 Kato, Y.: Hydrothermal ferromanganese oxides around a petit-spot volcano on old and cold
881 oceanic crust, *Commun. Earth Environ.*, *4*, 191, [https://doi.org/10.1038/s43247-023-00832-](https://doi.org/10.1038/s43247-023-00832-3)
882 [3](https://doi.org/10.1038/s43247-023-00832-3), 2023.
- 883 Bell, K. and Tilton, G. R.: Probing the mantle: the story from carbonatites, *Eos*, *83*, 273–277,
884 <https://doi.org/10.1029/2002EO000190>, 2002.
- 885 Bellas, A., Zhong, S. and Watts, A.B.: Reconciling lithospheric rheology between laboratory
886 experiments, field observations and different tectonic settings, *Geophys. J. Int.*, *228*, 857–
887 875, <https://doi.org/10.1093/gji/ggab382>, 2022.
- 888 Bianco, T.A, Ito, G., Becker, J.M. and Garcia, M.O.: Secondary Hawaiian volcanism formed by
889 flexural arch decompression, *Geochem. Geophys. Geosyst.* *6*, Q08009,
890 <https://doi.org/10.1029/2005GC000945>, 2005.
- 891 Bizimis, M., Salters, V.J.M. and Dawson, J.B.: The brevity of carbonatite sources in the mantle:
892 evidence from Hf isotopes, *Contrib. to Mineral. Petrol.*, *145*, 281–300,



- 893 <https://doi.org/0.1007/s00410-003-0452-3>, 2003.
- 894 Bizimis, M., Salters, V.J.M., Garcia, M.O. and Norman, M.D.: The composition and distribution of
895 the rejuvenated component across the Hawaiian plume: Hf-Nd-Sr-Pb isotope systematics of
896 Kaula lavas and pyroxenite xenoliths, *Geochem. Geophys. Geosyst.* 14, 4458–4478,
897 <https://doi.org/10.1002/ggge.20250>, 2013.
- 898 Borsova, A.Y. and Tilhac, R.: Derivation of Hawaiian rejuvenated magmas from deep carbonated
899 mantle sources: A review of experimental and natural constraints, *Earth. Sci. Rev.*, 222,
900 103819, <https://doi.org/10.1016/j.earscirev.2021.103819>, 2021.
- 901 Brenna, M., Ubide, T., Nichols, A.R.L., Mollo, S. and Pontesilli, A.: Anatomy of intraplate
902 monogenetic alkaline basaltic magmatism: clues from magma, crystals and glass, *Crustal
903 Magmat. Syst. Evol. Anat. Archit. Physico-Chemical Process.*, 79–103,
904 <https://doi.org/10.1002/9781119564485.ch4>, 2021.
- 905 Buchs, D.M., Pilet, S., Cosca, M., Flores, K.E., Bandini, A.N. and Baumgartner, P.O.: Low-volume
906 intraplate volcanism in the Early/Middle Jurassic Pacific basin documented by accreted
907 sequences in Costa Rica, *Geochem. Geophys. Geosyst.*, 14, 1552–1568,
908 <https://doi.org/10.1002/ggge.20084>, 2013.
- 909 Carnevale, G., Caracausi, A., Correale, A., Italiano, L. and Rotolo, S.G.: An Overview of the
910 Geochemical Characteristics of Oceanic Carbonatites: New Insights from Fuerteventura
911 Carbonatites (Canary Islands), *Minerals*, 11, 203, <https://doi.org/10.3390/min11020203>,
912 2021.
- 913 Chantel, J., Manthilake, G., Andrault, D., Novella, D., Yu, T. and Wang, Y.: Experimental evidence
914 supports mantle partial melting in the asthenosphere, *Sci. Adv.*, 2, e1600246,
915 <https://doi.org/10.1126/sciadv.1600246>, 2016.
- 916 Chen, X., Wang, M., Inoue, T., Liu, Q., Zhang, L. and Bader, T.: Melting of carbonated pelite at 5.5–
917 15.5 GPa: implications for the origin of alkali-rich carbonatites and the deep water and
918 carbon cycles, *Contrib. to Mineral. Petrol.*, 177, 2, [https://doi.org/10.1007/s00410-021-
919 01867-5](https://doi.org/10.1007/s00410-021-01867-5), 2022.
- 920 Clague, D.A. and Frey, F.A.: Petrology and Trace element Geochemistry of the Honolulu Volcanics,
921 Oahu: Implications for the Oceanic Mantle below Hawaii, *J. Petrol.*, 23, 447–504,
922 <https://doi.org/10.1093/petrology/23.3.447>, 1982.
- 923 Clague, D.A., Holcomb, R.T., Sinton, J.M., Detrick, R.S. and Torresan, M.E.: Pliocene and
924 Pleistocene alkali flood basalts on the seafloor north of the Hawaiian island, *Earth Planet.
925 Sci. Lett.*, 98, 175–191, [https://doi.org/10.1016/0012-821X\(90\)90058-6](https://doi.org/10.1016/0012-821X(90)90058-6), 1990.
- 926 Clague, D.A., Moore, J.G.: The proximal part of the giant submarine Wailau landslide, Molokai,
927 Hawaii, *J. Volcanol. Geotherm. Res.*, 113, 259–287, [https://doi.org/10.1016/S0377-
928 0273\(01\)00261-X](https://doi.org/10.1016/S0377-0273(01)00261-X), 2002.



- 929 Collerson, K.D., Williams, Q., Ewart, A.E. and Murphy, D.T.: Origin of HIMU and EM-1 domains
930 sampled by ocean island basalts, kimberlites and carbonatites: The role of CO₂-fluxed lower
931 mantle melting in thermochemical upwellings, *Phys. Earth Planet. Inter.*, 181, 112–131,
932 <https://doi.org/10.1016/j.pepi.2010.05.008>, 2010.
- 933 Conrad, C.P., Bianco, T.A., Smith, E.I. and Wessel, P.: Patterns of intraplate volcanism controlled by
934 asthenospheric shear. *Nat. Geosci.*, 4, 317–321, <https://doi.org/10.1038/ngeo1111>, 2011.
- 935 Cousens, B.L. and Clague, D.A.: Shield to Rejuvenated Stage Volcanism on Kauai and Niihau,
936 Hawaiian Islands, *J. Petrol.*, 56, 1547–1584, <https://doi.org/10.1093/petrology/egv045>,
937 2015.
- 938 Dasgupta, R. and Hirschmann, M.M.: Melting in the Earth's deep upper mantle caused by carbon
939 dioxide, *Nature*, 440, 659–662, <https://doi.org/10.1038/nature04612>, 2006.
- 940 Dasgupta, R., Hirschmann, M.M. and Stalker, K.: Immiscible Transition from Carbonate-rich to
941 Silicate-rich Melts in the 3 GPa Melting Interval of Eclogite + CO₂ and Genesis of Silica-
942 undersaturated Ocean Island Lavas, *J. Petrol.*, 47, 647–671,
943 <https://doi.org/10.1093/petrology/egi088>, 2006.
- 944 Dasgupta, R., Hirschmann, M.M. and Smith, N.D.: Partial Melting Experiments of Peridotite + CO₂
945 at 3 GPa and Genesis of Alkalic Ocean Island Basalts, *J. Petrol.*, 48, 2093–2124,
946 <https://doi.org/10.1093/petrology/egm053>, 2007.
- 947 Dasgupta, R., Hirschmann, M.M., McDonough, W.F., Spiegelman, M. and Withers, A.: Trace
948 element partitioning between garnet lherzolite and carbonatite at 6.6 and 8.6 GPa with
949 applications to the geochemistry of the mantle and of mantle-derived melts, *Chem. Geol.*,
950 262, 57–77, <https://doi.org/10.1016/j.chemgeo.2009.02.004>, 2009.
- 951 Dasgupta, R., Mallik, A., Tsuno, K., Withers, A.C., Hirth, G. and Hirschmann, M.M.: Carbon-
952 dioxide-rich silicate melt in the Earth's upper mantle, *Nature*, 493, 211–215,
953 <https://doi.org/10.1038/nature11731>, 2013.
- 954 Debayle, E., Bodin, T., Durand, S. and Ricard, Y.: Seismic evidence for partial melt below tectonic
955 plates, *Nature*, 586, 555–559, <https://doi.org/10.1038/s41586-020-2809-4>, 2020.
- 956 Dixon, J., Clague, D.A., Cousens, B., Monsalve, M.L. and Uhl, J.: Carbonatite and silicate melt
957 metasomatism of the mantle surrounding the Hawaiian plume: evidence from volatiles, trace
958 elements, and radiogenic isotopes in rejuvenated-stage lavas from Niihau, Hawaii,
959 *Geochem. Geophys. Geosyst.*, 9, Q09005, <https://doi.org/10.1029/2008GC002076>, 2008.
- 960 Ebisawa, N., Sumino, H., Okazaki, R., Takigami, Y., Hirano, N., Nagao, K. and Kaneoka, I.:
961 Construction of I-Xe and ⁴⁰Ar-³⁹Ar dating system using a modified VG3600 noble gas mass
962 spectrometer and the first I-Xe data obtained in Japan, *J. Mass Spectrom. Soc. Jpn.*, 52,
963 219–229, <https://doi.org/10.5702/massspec.52.219>, 2004.
- 964 Falloon, T.J. Hoernle, K., Schaefer, B.F., Bindeman, I.N., Hart, S.R., Garbe-Schonberg, D. and



- 965 Duncan, R.A.: Petrogenesis of Lava from Christmas Island, Northeast Indian Ocean:
966 Implications for the Nature of Recycled Components in Non-Plume Intraplate Settings,
967 *Geosci.*, 12, 118, <https://doi.org/10.3390/geosciences12030118>, 2022.
- 968 Frey, F.A., Green, D.H. and Roy, S.D.: Integrated Models of Basalt Petrogenesis: A Study of Quartz
969 Tholeiites to Olivine Melilitites from South Eastern Australia Utilizing Geochemical and
970 Experimental Petrological Data, *J. Petrol.*, 19, 463–513,
971 <https://doi.org/10.1093/PETROLOGY/19.3.463>, 1978.
- 972 Frey, F.A., Clague, D., Mahoney, J.J. and Sinton, J.M.: Volcanism at the edge of the Hawaiian
973 plume: Petrogenesis of submarine alkali lavas from the North Arch volcanic field, *J. Petrol.*,
974 41, 667–691, <https://doi.org/10.1093/petrology/41.5.667>, 2000.
- 975 Fujie, G., Kodaira, S., Nakamura, Y., Morgan, J.P. Dannowski, A., Thorwart, M., Grevemeyer, I. and
976 Miura, S.: Spatial variations of incoming sediments at the northeastern Japan arc and their
977 implications for megathrust earthquakes, *Geology*, 48, 614–619,
978 <https://doi.org/10.1130/G46757.1>, 2020.
- 979 Fujiwara, T., Hirano, N. Abe, N. and Takizawa, K.: Subsurface structure of the “petit-spot”
980 volcanoes on the northwestern Pacific Plate, *Geophys. Res. Lett.*, 34, L13305,
981 <https://doi.org/10.1029/2007GL030439>, 2007.
- 982 Garcia, M.O., Weis, D., Jicha, B.R., Ito, G. and Hanano, D.: Petrology and geochronology of lavas
983 from Ka’ula Volcano: Implications for rejuvenated volcanism of the Hawaiian mantle
984 plume, *Geochim. Cosmochim. Acta.*, 185, 278–301,
985 <https://doi.org/10.1016/j.gca.2016.03.025>, 2016.
- 986 Ghosh, S., Ohtani, E., Litasov, K.K. and Terasaki, H.: Solidus of carbonated peridotite from 10 to 20
987 GPa and origin of magnesiocarbonatite melt in the Earth's deep mantle, *Chem. Geol.*, 262,
988 17–28, <https://doi.org/10.1016/j.chemgeo.2008.12.030>, 2009.
- 989 Grassi, D. and Schmidt, M.W.: The Melting of Carbonated Pelites from 70 to 700 km Depth, *J.*
990 *Petrol.*, 52, 765–789, <https://doi.org/10.1093/petrology/egr002>, 2011.
- 991 Gripp, A.E. and Gordon, R.G.: Current plate velocities relative to the hotspots incorporating the
992 NUVEL-1 global plate motion model, *Geophys. Res. Lett.*, 17, 1109–1112,
993 <https://doi.org/10.1029/GL017i008p01109>, 1990.
- 994 Hammouda, T., Manthilake, G., Goncalves, P., Chantel, J., Guignard, J., Crichton, W. and Gaillard,
995 F.: Is There a Global Carbonate Layer in the Oceanic Mantle?, *Geophys. Res. Lett.*, 48,
996 e2020GL089752, <https://doi.org/10.1029/2020GL089752>, 2020.
- 997 Hanano, D., Scoates, J.S. and Weis, D.: Alteration mineralogy and the effect of acid-leaching on the
998 Pb-isotope systematics of ocean-island basalts, *Am. Mineral.*, 94, 17–26,
999 <https://doi.org/10.2138/am.2009.2845>, 2009.
- 1000 Hanyu, T., Tatsumi, Y., Senda, R., Miyazaki, T., Chang, Q., Hirahara, Y., Takahashi, T., Kawabata,



- 1001 H., Suzuki, K., Kimura, J-I. and Nakai, S.: Geochemical characteristics and origin of the
1002 HIMU reservoir: A possible mantle plume source in the lower mantle, *Geochem. Geophys.*
1003 *Geosyst.*, 12, Q0AC09, <https://doi.org/10.1029/2010GC003252>, 2011.
- 1004 Hanyu, T., Shimizu, K., Ushikubo, T., Kimura, J.-I., Chang, Q., Hamada, M., Ito, M., Iwamori, H.
1005 and Ishikawa, T.: Tiny droplets of ocean island basalts unveil Earth's deep chlorine cycle,
1006 *Nat. Commun.*, 10, 60, <https://doi.org/10.1038/s41467-018-07955-8>, 2019.
- 1007 Hart, S.R.: A large-scale isotope anomaly in the Southern Hemisphere mantle, *Nature*, 309, 753–757,
1008 <https://doi.org/10.1038/309753a0>, 1984.
- 1009 Hart, S.R., Gerlach, D.C. and White, W.M.: A Possible new Sr-Nd-Pb mantle array and consequences
1010 for mantle mixing, *Geochim. Cosmochim. Acta.*, 50, 1551–1557,
1011 [https://doi.org/10.1016/0016-7037\(86\)90329-7](https://doi.org/10.1016/0016-7037(86)90329-7), 1986.
- 1012 Hein, J.R., Koschinsky, A., Bau, M., Manheim, F.T., Kang, J.K. and Roberts, L.: Cobalt-rich
1013 ferromanganese crusts in the Pacific, *Handbook of Marine Mineral Deposits* (Cronan DS,
1014 ed.), 239–279, CRC Press, Boca Raton, Florida, 1999.
- 1015 Helz, R.T. and Thronber, C.R.: Geochemistry of Kilauea Iki lava lake, Hawaii, *Bull. Volcanol.*, 49,
1016 651–658, <https://doi.org/10.1007/BF01080357>, 1987.
- 1017 Herath, P., Stern, T.A., Savage, M.K., Bassett, D. and Henrys, S.: Wide-angle seismic reflections
1018 reveal a lithosphere-asthenosphere boundary zone in the subducting Pacific Plate, New
1019 Zealand, *Sci. Adv.*, 8, eabn5697, <https://doi.org/10.1126/sciadv.abn5697>, 2022.
- 1020 Herzberg, C.: Petrology and thermal structure of the Hawaiian plume from Mauna Kea volcano,
1021 *Nature*, 444, 605–609. <https://doi.org/10.1038/nature05254>, 2006.
- 1022 Herzberg, C.: Identification of Source Lithology in the Hawaiian and Canary Islands: Implications
1023 for Origins, *J. Petrol.*, 52, 113–146, <https://doi.org/10.1093/petrology/egq075>, 2011.
- 1024 Hirano, N., Takahashi, E., Yamamoto, J., Abe, N., Ingle, S.P., Kaneoka, I., Hirata, T., Kimura, J.-I.,
1025 Ishii, T., Ogawa, Y., Machida, S. and Suyehiro, K.: Volcanism in response to plate flexure.
1026 *Science*, 313, 1426–1428. <https://doi.org/10.1126/science.1128235>, 2006.
- 1027 Hirano, N.: Petit-spot volcanism: a new type of volcanic zone discovered near a trench, *Geochem. J.*,
1028 45, 157–167, <https://doi.org/10.2343/geochemj.1.0111>, 2011.
- 1029 Hirano, N., Machida, S., Abe, N., Morishita, T., Tamura, A. and Arai, S.: Petit-spot lava fields off the
1030 central Chile trench induced by plate flexure, *Geochem. J.*, 47, 249–257,
1031 <https://doi.org/10.2343/geochemj.2.0227>, 2013.
- 1032 Hirano, N., Nakanishi, M., Abe, N. and Machida, S.: Submarine lava fields in French Polynesia,
1033 *Mar. Geol.*, 373, 39–48, <http://dx.doi.org/10.1016/j.margeo.2016.01.002>, 2016.
- 1034 Hirano, N., Machida, S., Sumino, H., Shimizu, K., Tamura, A., Morishita, T., Iwano, H., Sakata, S.,
1035 Ishii, T., Arai, S., Yoneda, S., Danhara, T. and Hirata, T.: Petit-spot volcanoes on the oldest
1036 portion of the Pacific Plate, *Deep Sea Res. Part I*, 154, 103142,



- 1037 <https://doi.org/10.1016/j.dsr.2019.103142>, 2019.
- 1038 Hirano, N., Sumino, H., Morishita, T., Machida, S., Kawano, T., Yasukawa, K., Hirata, T., Kato, Y.
1039 and Ishii, T.: A Paleogene magmatic overprint on Cretaceous seamounts of the western
1040 Pacific, *Island Arc*, 30, e12386, <https://doi.org/10.1111/iar.12386>, 2021.
- 1041 Hirano, N. and Machida, S.: The mantle structure below petit-spot volcanoes, *Commun. Earth*
1042 *Environ.*, 3, 110, <https://doi.org/10.1038/s43247-022-00438-1>, 2022.
- 1043 Hirth, G. and Kohlstedt, D.L.: Water in the oceanic upper mantle: implications for rheology, melt
1044 extraction and the evolution of the lithosphere. *Earth Planet. Sci. Lett.*, 144, 93–108,
1045 [https://doi.org/10.1016/0012-821X\(96\)00154-9](https://doi.org/10.1016/0012-821X(96)00154-9), 1996.
- 1046 Hoernle, K., Tilton, G., Le Bas, M.J., Duggem, S. and Garbe-Schönberg, D.: Geochemistry of
1047 oceanic carbonatites compared with continental carbonatites: mantle recycling of oceanic
1048 crustal carbonate, *Contrib. to Mineral. Petrol.*, 142, 520–542,
1049 <https://doi.org/10.1007/s004100100308>, 2002.
- 1050 Hoffman, A.W.: Mantle geochemistry: the message from oceanic volcanism, *Nature*, 385, 219–229,
1051 <https://doi.org/10.1038/385219a0>, 1997.
- 1052 Hoffman, A.W.: Sampling mantle heterogeneity through oceanic basalts: isotopes and trace
1053 elements. In: Carson, R. W. (Ed.), *Treatise on Geochemistry*, 2, The Mantle and Core,
1054 Elsevier, 61–101, <https://doi.org/10.1016/B0-08-043751-6/02123-X>, 2003.
- 1055 Hosseini, K., Matthews, K.J., Sigloch, K., Shephard, G.E., Domeier, M. and Tsekhmistrenko, M.:
1056 SubMachine: Web-Based tools for exploring seismic tomography and other models of
1057 Earth's deep interior, *Geochem. Geophys. Geosyst.*, 19, 1464–1483,
1058 <https://doi.org/10.1029/2018GC007431>, 2018.
- 1059 Hua, J., Fisher, K. M., Becker, T.W., Gazel, E. and Hirth, G.: Asthenospheric low-velocity zone
1060 consistent with globally prevalent partial melting, *Nat. Geosci.*, 16, 175–181,
1061 <https://doi.org/10.1038/s41561-022-01116-9>, 2023.
- 1062 Hulett, S.R., Simonetti, A., Rasbury, E.T. and Hemming, N.G.: Recycling of subducted crustal
1063 components into carbonatite melts revealed by boron isotopes, *Nat. Geosci.*, 9, 904–908,
1064 <https://doi.org/10.1038/ngeo2831>, 2016.
- 1065 Irving, A.J. and Green, D.H.: Geochemistry and petrogenesis of the newer basalts of Victoria and
1066 South Australia, *J. Geol. Sci. Australia*, 23, 45–66,
1067 <https://doi.org/10.1080/00167617608728920>, 1976.
- 1068 Iwata, N.: Geochronological study of the Deccan volcanism by the ^{40}Ar – ^{39}Ar method, Doctor
1069 Thesis, University of Tokyo, pp. 168, 1998.
- 1070 Jochum, K.P. and Nohl, U.: Reference materials in geochemistry and environmental research and the
1071 GeoReM database, *Chem. Geol.*, 253, 50–53,



- 1072 <https://doi.org/10.1016/j.chemgeo.2008.04.002>, 2008.
- 1073 Johnson, K.T.M., Dick, H.J.B. and Shimizu, N.: Melting in the oceanic upper mantle: An ion
1074 microprobe study of diopsides in abyssal peridotites, *J. Geophys. Res.*, 95, 2661–2678,
1075 <https://doi.org/10.1029/JB095iB03p02661>, 1990.
- 1076 Juriček, M.P and Keppler, H.: Amphibole stability, water storage in the mantle, and the nature of the
1077 lithosphere-asthenosphere boundary, *Earth Planet. Sci. Lett.*, 608, 118082,
1078 <https://doi.org/10.1016/j.epsl.2023.118082>, 2023.
- 1079 Kaneko, J., Machida, S., Hirano, N., Kasaya, T. and Kumagai, H.: Near bottom MBES survey
1080 mounted on a HOV at 5500m depth. *Oceans Conference Record (IEEE) 2022*, 1–5,
1081 <https://doi.org/10.1109/OCEANSCennai45887.2022.9775366>, 2022.
- 1082 Karato, S.-I. and Jung, H.: Water, partial melting and the origin of the seismic low velocity and high
1083 attenuation zone in the upper mantle, *Earth Planet. Sci. Lett.*, 157, 193–207,
1084 [https://doi.org/10.1016/S0012-821X\(98\)00034-X](https://doi.org/10.1016/S0012-821X(98)00034-X), 1998.
- 1085 Katsura, T. and Fei, H.: Asthenosphere dynamics based on the H₂O dependence of element
1086 diffusivity in olivine, *Natl. Sci. Rev.*, 8, nwaa278. <https://doi.org/10.1093/nsr/nwaa278>,
1087 2020.
- 1088 Kawakatsu, H., Kumar, P., Takei, Y., Shinohara, M., Kanazawa, T., Araki, E. and Suyehiro, K.:
1089 Seismic Evidence for Sharp Lithosphere-Asthenosphere Boundaries of Oceanic Plates,
1090 *Science*, 324, 499–502, <https://www.science.org/doi/10.1126/science.1169499>, 2009.
- 1091 Kelemen, P.B., Yogodzinskim G.M., and Scholl, D.W.: Along-strike variation in the Aleutian Island
1092 Arc: genesis of high Mg# andesite and implications for continental crust, In: Eiler, J. (ed.),
1093 *Inside the subduction Factory*, American Geophysical Union, Geophysical Monograph, 138,
1094 223–276, <https://doi.org/10.1029/138GM11>, 2003.
- 1095 Keshav, S. and Gudfinnsson, G.H.: Silicate liquid-carbonatite liquid transition along the melting curve
1096 of model, vapor-saturated peridotite in the system CaO-MgO-Al₂O₃-SiO₂-CO₂ from 1.1 to
1097 2 GPa, *J. Geophys. Res.*, 118, 3341–3353, <https://doi.org/10.1002/jgrb.50249>, 2013.
- 1098 Kiseeva, E.S., Litasov, K.D., Yaxley, G.M., Ohtani, E. and Kamenetsky, V.S.: Melting and Phase
1099 Relations of Carbonated Eclogite at 9–21 GPa and the Petrogenesis of Alkali-Rich Melts in
1100 the Deep Mantle, *J. Petrol.*, 54, 1555–1583, <https://doi.org/10.1093/petrology/egt023>, 2013.
- 1101 Kobayashi, M., Sumino, H., Saito, T., Nagao, K.: Determination of halogens in geological reference
1102 materials using neutron irradiation noble gas mass spectrometry, *Chem. Geol.*, 582, 120420,
1103 <https://doi.org/10.1016/j.chemgeo.2021.120420>, 2021.
- 1104 Konovalov, Y. I. and Martynov, Y. A.: Volcanic complex of the La Mont Guyot; Marcus-Wake Uplift,
1105 *Pacific Ocean, Pacific Geology*, 5, 40–47, 1992.
- 1106 Konter, J.G., Hanan, B.B., Blicher-Toft, J., Koppers, A.A.P., Plank, T. and Staudigel, H.: One
1107 hundred million years of mantle geochemical history suggest the retiring of mantle plumes



- 1108 is premature, *Earth Planet Sci Lett*, 275, 285–295,
1109 <https://doi.org/10.1016/j.epsl.2008.08.023>, 2008.
- 1110 Koppers, A.A.P., Staudigel, H., Pringle, M.S. and Wijbrans, J.R.: Short-lived and discontinuous
1111 intra-plate volcanism in the South Pacific: hotspots or extensional volcanism?, *Geochem.*
1112 *Geophys. Geosyst.*, 4, 1089, <https://doi.org/10.1029/2003GC000533>, 2003.
- 1113 Korenaga, J.: Plate tectonics and surface environment: Role of the oceanic upper mantle, *Earth Sci.*
1114 *Rev.*, 205, 103185, <https://doi.org/10.1016/j.earscirev.2020.103185>, 2020.
- 1115 Le Bas, M. J., Le Maitre, R., Strackeisen, A. and Zanettin, B. (1986) A chemical classification of
1116 volcanic rocks based on the total alkali–silica diagram, *J. Petrol.*, 27, 745–750,
1117 <https://doi.org/10.1093/petrology/27.3.745>, 2020.
- 1118 Lei, J. and Zhao, D.: P-wave tomography and origin of the Changbai intraplate volcano in Northeast
1119 Asia, *Tectonophysics*, 397, 281–295. <https://doi.org/10.1016/j.tecto.2004.12.009>, 2005.
- 1120 Lu, C., Grand, S. P., Lai, H. and Garnero, E. J.: TX2019slab: A New P and S Tomography Model
1121 Incorporating Subducting Slabs, *J. Geophys. Res.*, 124, 11549–11567,
1122 <https://doi.org/10.1029/2019JB017448>, 2019.
- 1123 Liu, J., Hirano, N., Machida, S., Xia, Q., Tao, C., Liao, S., Liang, J., Li W., Yang, W. Zhang, G. and
1124 Ding, T.: Melting of recycled ancient crust responsible for the Gutenberg discontinuity, *Nat.*
1125 *Commun.*, 11, 172, <https://doi.org/10.1038/s41467-019-13958-w>, 2020.
- 1126 Longerich, H.P., Jackson, S.E. and Gunther, D.: Laser ablation inductively coupled plasma mass
1127 spectrometric transient signal data acquisition and analyte concentration calculation, *J. Anal.*
1128 *At. Spectrom.*, 11, 899–904, <https://doi.org/10.1039/ja9961100899>, 1996.
- 1129 Machida, S., Hirano, N., and Kimura, J.-I.: Evidence for recycled material in Pacific upper mantle
1130 unrelated to plumes, *Geochim. Cosmochim. Acta.*, 73, 3028–3037,
1131 <http://dx.doi.org/10.1016/j.gca.2009.01.026>, 2009.
- 1132 Machida, S., Orihashi, Y., Magnani, M., Neo, N., Wilson, S., Tanimizu, M., Yoneda, S., Yasuda, A.
1133 and Tamaki, K.: Regional mantle heterogeneity regulates melt production along the Réunion
1134 hotspot-influenced Central Indian Ridge, *Geochem. J.*, 48, 433–449,
1135 <https://doi.org/10.2343/geochemj.2.0320>, 2014.
- 1136 Machida, S., Hirano, N., Sumino, H., Hirata, T., Yoneda, S. and Kato, Y.: Petit-spot geology reveals
1137 melts in upper-most asthenosphere dragged by lithosphere, *Earth Planet. Sci. Lett.*, 426,
1138 267–279, <https://doi.org/10.1016/j.epsl.2015.06.018>, 2015
- 1139 Machida, S., Fujinaga, K., Ishii, T., Nakamura, K., Hirano, N. and Kato, Y.: Geology and
1140 geochemistry of ferromanganese nodules in the Japanese Exclusive Economic Zone around
1141 Minamitorishima Island, *Geochem. J.*, 50, 539–555,
1142 <https://doi.org/10.2343/geochemj.2.0419>, 2016.
- 1143 Machida, S., Kogiso, T. and Hirano, N.: Petit-spot as definitive evidence for partial melting in the



- 1144 asthenosphere caused by CO₂, *Nat. Commun.*, 8, 14302,
1145 <https://doi.org/10.1038/ncomms14302>, 2017.
- 1146 Massuyeau, M., Gardés, E., Morizet, Y. and Gaillard, F.: A model for the activity of silica along the
1147 carbonatite–kimberlite–mellilitite–basanite melt compositional joint, *Chem. Geol.*, 418,
1148 206–216, <https://doi.org/10.1016/j.chemgeo.2015.07.025>, 2015.
- 1149 McKenzie, D. and O’Nions, R.K.: Partial melt distributions from inversion of rare Earth element
1150 concentrations, *J. Petrol.*, 32, 1021–1091, <https://doi.org/10.1093/petrology/32.5.1021>,
1151 1991.
- 1152 Melson, W.G., Thompson, G. and van Andel, T.H.: Volcanism and metamorphism in the Mid-
1153 Atlantic Ridge, 22°N latitude, *J. Geophys. Res.*, 73, 5925–5941,
1154 <https://doi.org/10.1029/JB073i018p05925>, 1968.
- 1155 Mierdel, K., Keppler, H., Smyth, J.R. and Langenhorst, F.: Water solubility in aluminous
1156 orthopyroxene and the origin of Earth’s Asthenosphere, *Science*, 315, 364–368,
1157 <https://doi.org/10.1126/science.1135422>, 2007.
- 1158 Mikuni, K., Hirano, N., Akizawa, N., Yamamoto, J., Machida, S., Tamura, A., Hagiwara, Y.,
1159 Morishita, T.: Lithological structure of western Pacific lithosphere reconstructed from
1160 mantle xenoliths in a petit-spot volcano, *Prog. Earth Planet. Sci.*, 9, 62,
1161 <https://doi.org/10.1186/s40645-022-00518-y>, 2022.
- 1162 Miyashiro, A., Shido, F. and Ewing, M.: Metamorphism on the Mid-Atlantic Ridge near 24 and 30°
1163 N. *Phil. Trans. Roy. Soc. Lond.*, 268, 589–603, <https://doi.org/10.1098/rsta.1971.0014>,
1164 1971.
- 1165 Morimoto, N.: Nomenclature of pyroxenes. *Mineral. Petrol.*, 39, 55–76,
1166 <https://doi.org/10.1007/BF01226262>, 1988.
- 1167 Moore, J.G., Fornari, D.J. and Clague, D.A.: Basalts from the 1877 Submarine Eruption of Mauna
1168 Loa, Hawaii; New Data on the Variation of Palagonitization Rate with Temperature. *United*
1169 *States Geol. Surv. Bull.* 1663., 1–11, <https://doi.org/10.3133/b1663>, 1985.
- 1170 Müller, R.D., Sdrolias, M., Gaina, C. and Roest, W.R.: Age, spreading rates, and spreading
1171 asymmetry of the world’s ocean crust. *Geochem. Geophys. Geosyst.*, 9, Q04006.
1172 <http://dx.doi.org/10.1029/2007GC001743>, 2008.
- 1173 Natland, J.: Petrology of Volcanic Rocks Dredged from Seamounts in the Line Islands, *Init. Rep.*
1174 *Deep Sea Drill. Proj.*, 33, 749–777. <https://doi.org/10.2973/dsdp.proc.33.126.1976>, 1976.
- 1175 Nier, A.: A redetermination of the relative abundances of the isotopes of carbon, nitrogen, oxygen,
1176 argon, and potassium, *Phys. Rev.*, 77, 789–793, <https://doi.org/10.1103/PhysRev.77.789>,
1177 1950.
- 1178 Nobre Silva, I.G., Weis, D., Barling, J. and Scoates, J.S.: Leaching systematics and matrix
1179 elimination for the determination of high-precision Pb isotope compositions of ocean island



- 1180 basalts, *Geochem. Geophys. Geosyst.*, 10, Q08012, <https://doi.org/10.1029/2009GC002537>,
1181 2009.
- 1182 Novella, D., Keshav, S., Gudfinnsson, G.H. and Ghosh, S.: Melting phase relations of model
1183 carbonated peridotite from 2 to 3 GPa in the system CaO-MgO-Al₂O₃-SiO₂-CO₂ and further
1184 indication of possible unmixing between carbonatite and silicate liquids, *J. Geophys. Res.*,
1185 119, 2780–2800, <https://doi.org/10.1002/2013JB010913>, 2014.
- 1186 Nozaki, T., Tokumaru, A., Takaya, Y., Kato, Y., Suzuki, K. and Urabe, T.: Major and trace element
1187 compositions and resource potential of ferromanganese crust at Takuyo Daigo Seamount,
1188 northwestern Pacific Ocean, *Geochem J.*, 50, 527–537,
1189 <https://doi.org/10.2343/geochemj.2.0430>, 2016.
- 1190 Ohtani, E and Zhao, D.: The role of water in the deep upper mantle and transition zone: dehydration
1191 of stagnant slabs and its effects on the big mantle wedge, *Russ. Geol. Geophys.*, 50, 1073–
1192 1078, <https://doi.org/10.1016/j.rgg.2009.11.006>, 2009.
- 1193 Okumura, S. and Hirano, N.: Carbon dioxide emission to earth's surface by deep-sea volcanism,
1194 *Geology*, 41, 1167–1170, <https://doi.org/10.1130/G34620.1>, 2013.
- 1195 Orihashi, Y., Maeda, J., Tanaka, R., Zeniya, R. and Niida, K.: Sr and Nd isotopic data for the seven
1196 GSJ rock reference samples; JA-1, JB-1a, JB-2, JB-3, JG-1a, JGb-1 and JR-1, *Geochem. J.*,
1197 32, 205–211, <https://doi.org/10.2343/geochemj.32.205>, 1998.
- 1198 Ozawa, K.: Mass balance equations for open magmatic systems: Trace element behavior and its
1199 application to open system melting in the upper mantle. *J. Geophys. Res.*, 106, 13407–
1200 13434, <https://doi.org/10.1029/2001JB900001>, 2001.
- 1201 Pearce, N.J.G., Perkins, W.T., Westgate, J.A., Gorton, M.P., Jackson, S.E., Neal, C.R. and Chenery,
1202 S.P.: A compilation of new and published major and trace element data for NIST SRM 610
1203 and NIST SRM 612 glass reference materials, *Geostand. Newsl.*, 21, 115–144,
1204 <https://doi.org/10.1111/j.1751-908X.1997.tb00538.x>, 1997.
- 1205 Pilet, S., Baker, M.B. and Stolper, E.M.: Metasomatized Lithosphere and the Origin of Alkaline
1206 Lavas, *Science*, 320, 916–919, <https://doi.org/10.1126/science.1156>, 2008.
- 1207 Pilet, S.: Generation of low-silica alkaline lavas: Petrological constrains, models, and thermal
1208 implications, *The Interdisciplinary Earth: A Volume in Honor of Don L. Anderson*, Gillian
1209 R. Foulger, Michele Lustrino, Scott D. King. [https://doi.org/10.1130/2015.2514\(17\)](https://doi.org/10.1130/2015.2514(17)), 2015.
- 1210 Pilet, S., Abe, N., Rochat, L., Kaczmarek, M.-A., Hirano, N., Machida, S., Buchs, D.M.,
1211 Baumgarther, P.O. and Müntener, O.: Pre-subduction metasomatic enrichment of the oceanic
1212 lithosphere induced by plate flexure, *Nat. Geosci.*, 9, 898–903,
1213 <https://doi.org/10.1038/ngeo2825>, 2016.
- 1214 Regelous, M., Weinzierl, C.G. and Haase, K.M.: Controls on melting at spreading ridges from
1215 correlated abyssal peridotite – mid-ocean ridge basalt compositions, *Earth Planet. Sci. Lett.*,



- 1216 449, 1–11. <http://dx.doi.org/10.1016/j.epsl.2016.05.017>, 2016.
- 1217 Reinhard, A.A., Jackson, M.G., Blusztajn, J., Koppers, A.A.P., Simms, A.R. and Konter, J.G.: “Petit
1218 Spot” Rejuvenated Volcanism Superimposed on Plume-Derived Samoan Shield Volcanoes:
1219 Evidence From a 645-m Drill Core From Tutuila Island, American Samoa, *Geochem.*
1220 *Geophys. Geosys.*, 20, 1485–1507, <https://doi.org/10.1029/2018GC007985>, 2019.
- 1221 Resing, J.A. and Sansone, F.J.: The chemistry of lava–seawater interactions: the generation of
1222 acidity, *Geochim. Cosmochim. Acta.*, 63, 2183–2198, [https://doi.org/10.1016/S0016-7037\(99\)00193-3](https://doi.org/10.1016/S0016-7037(99)00193-3), 1999.
- 1224 Rohrbach, A., Ballhaus, C., Golla-Schindler, U., Ulmer, P., Kamenetsky, V.S. and Kuzmin, D.V.:
1225 Metal saturation in the upper mantle, *Nature*, 449, 456–458,
1226 <https://doi.org/10.1038/nature06183>, 2007.
- 1227 Sakamaki, T., Suzuki, A., Ohtani, E., Terasaki, H., urakawa, S., Katayama, Y., Funakoshi, K.-I.,
1228 Wang, Y. Hernlund, J.H. and Ballmer, M.D.: Ponded melt at the boundary between the
1229 lithosphere and asthenosphere, *Nat. Geosci.*, 6, 1041–1044,
1230 <https://doi.org/10.1038/ngeo1982>, 2013.
- 1231 Shaw, D.M.: Trace element fractionation during anataxis, *Geochim. Cosmochim. Acta.*, 34, 237–
1232 243, [https://doi.org/10.1016/0016-7037\(70\)90009-8](https://doi.org/10.1016/0016-7037(70)90009-8), 1970.
- 1233 Shaw, C.S.J.: Dissolution of orthopyroxene in basanitic magma between 0.4 and 2 GPa: Further
1234 implications for the origin of Si–rich alkaline glass inclusions in mantle xenoliths, *Contrib.*
1235 *Mineral. Petrol.*, 135, 114–132, <https://doi.org/10.1007/s004100050501>, 1999.
- 1236 Sifré, D., Gardés, E., Massuyeau, M., Hashim, L., Hier-Majumder, S. and Gaillard, F.: Electrical
1237 conductivity during incipient melting in the oceanic low-velocity zone, *Nature*, 509, 81–85,
1238 <https://doi.org/10.1038/nature13245>, 2014.
- 1239 Smith, W.H.F., Staudigel, H., Watts, A.B. and Pringle, M.S.: The Magellan seamounts: early
1240 Cretaceous record of the South Pacific isotopic and thermal anomaly, *J. Geophys. Res.*, 94,
1241 10501–10523, <https://doi.org/10.1029/JB094iB08p10501>, 1989.
- 1242 Staudigel, H. and Hart, S.R.: Alteration of basaltic glass: processes and significance for the oceanic
1243 crust-seawater budget, *Geochim. Cosmochim. Acta.*, 47, 337–350,
1244 [https://doi.org/10.1016/0016-7037\(83\)90257-0](https://doi.org/10.1016/0016-7037(83)90257-0), 1983.
- 1245 Staudigel, H., Park, K.H., Pringle, M., Rubenstone, J.L., Smith, W.H.F. and Zindler, A.: The
1246 longevity of the South-Pacific isotopic and thermal anomaly, *Earth Planet. Sci. Lett.*, 102,
1247 24–44, [https://doi.org/10.1016/0012-821X\(91\)90015-A](https://doi.org/10.1016/0012-821X(91)90015-A), 1991.
- 1248 Stixrude, L. and Lithgow-Bertelloni, C.: Thermodynamics of mantle minerals — I. Physical
1249 properties, *Geophys. J. Int.*, 162, 610–632, <https://doi.org/10.1111/j.1365-246X.2005.02642.x>, 2005.
- 1251 Stoenner, R.W., Schaeffer, O.A. and Katcoff, S.: Half-lives of argon-37, argon-39, and argon-42,



- 1252 Science, 148, 1325–1328, <https://doi.org/10.1126/science.148.3675.1325>, 1965.
- 1253 Stracke A., Michael, W., Felix, G., Paul, B. and Erin, T.: Major and trace element concentrations and
1254 Sr, Nd, Hf, Pb isotope ratios of global mid ocean ridge and ocean island basalts, GRO data,
1255 V1, <https://doi.org/10.25625/OSVW6S>, 2022.
- 1256 Sun, S.-S. and McDonough, W.F.: Chemical and isotopic systematics of oceanic basalts: implications
1257 for mantle composition and processes, *Geol. Soc. Spec. Publ.*, 42, 313–345,
1258 <https://doi.org/10.1144/GSL.SP.1989.042.01.19>, 1989.
- 1259 Takahashi, E.: Origin of basaltic magmas: Implications from peridotite melting experiments and an
1260 olivine fractionation model (in Japanese with English abstract), *Bull. Volcanol. Soc. Jpn.*,
1261 2nd Ser, 30, S17–S40, https://doi.org/10.18940/kazanc.30.TOKUBE_S17, 1986.
- 1262 Takahashi, E., Uto, K. and Schilling, J.-G.: Primary magma compositions and Mg/Fe ratios of their
1263 mantle residues along Mid Atlantic Ridge 29° N to 73°N, Technical Report of ISEI
1264 Okayama University Series A, 9, 1–4, 1987.
- 1265 Tamura, A., Arai, S., Takeuchi, M., Miura, M. and Pirnia, T.: Compositional heterogeneity of a
1266 websterite xenolith from Kurose, southwest Japan: insights into the evolution of lower crust
1267 beneath the Japan Arc, *Eur. J. Mineral.*, 31, 35–47, [https://doi.org/10.1127/ejm/2018/0030-](https://doi.org/10.1127/ejm/2018/0030-2803)
1268 2803, 2019.
- 1269 Taneja, R., Rushmer, T., Blichert-Toft, J., Turner, S. and O'Neill, C.: Mantle heterogeneities beneath
1270 the Northeast Indian Ocean as sampled by intra-plate volcanism at Christmas Island, *Lithos*,
1271 262, 561–575, <http://dx.doi.org/10.1016/j.lithos.2016.07.027>, 2016.
- 1272 Tanimizu, M. and Ishikawa, T.: Development of rapid and precise Pb isotope analytical techniques
1273 using MC-ICPMS and new results for GSJ rock reference samples, *Geochem. J.*, 40, 121–
1274 133. <https://doi.org/10.2343/geochemj.40.121>, 2006.
- 1275 Tatsumi, Y., Sakuyama, M., Fukuyama, H. and Kushiro, I.: Generation of arc basalt magmas and
1276 thermal structure of the mantle wedge in subduction zones, *J. Geophys. Res.*, 88, 5815–
1277 5825, <https://doi.org/10.1029/JB088iB07p05815>, 1983.
- 1278 Tivey, M.A., Sager, W.W., Lee, S.-M. and Tominaga, M.: Origin of the Pacific Jurassic quiet zone,
1279 *Geology*, 34, 789–792, <https://doi.org/10.1130/G22894.1>, 2006.
- 1280 Uenzelmann-Neben, G., Schmidt, D.N., Niessen, F. and Stein, R.: Intraplate volcanism off South
1281 Greenland: caused by glacial rebound?, *Geophys. J. Int.*, 190, 1–7,
1282 <https://doi.org/10.1111/j.1365-246X.2012.05468.x>, 2012.
- 1283 Valentine, G.A. and Hirano, N.: Mechanisms of low-flux intraplate volcanic fields—Basin and
1284 Range (North America) and northwest Pacific Ocean, *Geology*, 38, 55–58,
1285 <https://doi.org/10.1130/G30427.1>, 2010.
- 1286 Walter, M.J.: Melting of garnet peridotite and the origin of komatiite and depleted lithosphere, *J.*
1287 *Petrol.*, 39, 29–60, <https://doi.org/10.1093/etroj/39.1.29>, 1998.



- 1288 Wakaki, S., Shibata, S.-N. and Tanaka, T.: Isotope ratio measurements of trace Nd by the total
1289 evaporation normalization (TEN) method in thermal ionization mass spectrometry, *Int. J.*
1290 *Mass Spectrom.*, 264, 157–163, <http://dx.doi.org/10.1016/j.ijms.2007.04.006>, 2007.
- 1291 Wang, D., Mookherjee, M., Xu Y. and Karato, S.-I.: The effect of water on the electrical conductivity
1292 of olivine, *Nature*, 443, 977–980, <https://doi.org/10.1038/nature05256>, 2006.
- 1293 Wang, X.-J., Chen, L.-H., Hoffman, A.W., Hanyu, T., Kawabata, H., Zhong, Y., Xie, L.-W., Shi, J.-
1294 H., Miyazaki, T., Hirata, Y., Takahashi, T., Senda, R., Chang, O., Vaglarov, B.S. and Kimura,
1295 J.-I. Recycled ancient ghost carbonate in the Pitcairn mantle plume, *PNAS*, 115, 8682–8687,
1296 <https://doi.org/10.1073/pnas.1719570115>, 2018.
- 1297 Weis, D. and Frey, F.A.: Isotope geochemistry of the Ninetyeast Ridge basement basalts: Sr, Nd, and
1298 Pb evidence for involvement of the Kerguelen hot spot, *Proc. Ocean Drill. Program Sci.*
1299 *Results*, 121, 591–610, 1991.
- 1300 Weis, D. and Frey, F.A.: Role of the Kerguelen Plume in generating the eastern Indian Ocean
1301 seafloor. *J. Geophys. Res.*, 101, 13381–13849, <https://doi.org/10.1029/96JB00410>, 1996.
- 1302 Weis, D., Kieffer, B., Maerschalk, C., Barling, J., de Jong, J., Williams, G.A., Hanano, D., Pretorius,
1303 W., Mattielli, N., Scoates, J.S., Goolaerts, A., Friedman, R. M. and Mahoney, J.B.: High-
1304 precision isotopic characterization of USGS reference materials by TIMS and MC-ICP-MS,
1305 *Geochem. Geophys. Geosyst.*, 7, Q08006, <http://dx.doi.org/10.1029/2006GC001283>, 2006.
- 1306 Weiss, Y., Class, C., Goldstein, S.L. and Hanyu, T.: Key new pieces of the HIMU puzzle from
1307 olivines and diamond inclusions, *Nature*, 537, 666–670,
1308 <https://doi.org/10.1038/nature19113>, 2016.
- 1309 White, W.M.: *Geochemistry*, John Wiley & Sons., 2013.
- 1310 Workman, R.K., Hart, S.R., Jackson, M., Regelous, M., Farley, K.A., Blusztajn, J., Kurz, M. and
1311 Staudigel, H.: Recycled metasomatized lithosphere as the origin of the Enriched Mantle II
1312 (EM2) end-member: Evidence from the Samoan Volcanic Chain, *Geochem. Geophys.*
1313 *Geosyst.*, 5, Q04008, <https://doi.org/10.1029/2003GC000623>, 2004.
- 1314 Yamamoto, J., Hirano, N., Abe, N. and Hanyu, T.: Noble gas isotopic compositions of mantle
1315 xenoliths from northwestern Pacific lithosphere, *Chem. Geol.*, 268, 313–323,
1316 <https://doi.org/10.1016/j.chemgeo.2009.09.009>, 2009.
- 1317 Yamamoto, J., Korenaga, J., Hirano, N. and Kagi, H.: Melt-rich lithosphere-asthenosphere boundary
1318 inferred from petit-spot volcanoes, *Geology*, 42, 967–970,
1319 <https://doi.org/10.1130/G35944.1>, 2014.
- 1320 Yamamoto, J., Kawano, T., Takahata, N. and Sano, Y.: Noble gas and carbon isotopic compositions
1321 of petit-spot lavas from southeast of Marcus Island. *Earth Planet. Sci. Lett.*, 497, 139–148,
1322 <https://doi.org/10.1016/j.epsl.2018.06.020>, 2018.
- 1323 Yamamoto, J., Hirano, N. and Kurz, M.D.: Noble gas isotopic compositions of seamount lavas from



- 1324 the central Chile trench: Implications for petit-spot volcanism and the lithosphere
1325 asthenosphere boundary, *Earth Planet. Sci. Lett.*, 552, 116611,
1326 <https://doi.org/10.1016/j.epsl.2020.116611>, 2020.
- 1327 Yamazaki, S., Neo, N. and Miyashita, S.: Data report: whole-rock major and trace elements and
1328 mineral compositions of the sheeted dike–gabbro transition in ODP Hole 1256D, In Teagle,
1329 D. A. H., Alt, J. C., Umino, S., Miyashita, S., Banerjee, N. R., Wilson, D. S. and the
1330 Expedition 309/312 Scientists (Eds.), *Proceedings Integrated Ocean Drilling Program*.
1331 309/312: Washington, DC (Integrated Ocean Drilling Program Management International,
1332 Inc.) <https://doi.org/10.2204/iodp.proc.309312.203.2009>, 2009.
- 1333 Yang, H.-J., Frey, F.A. and Clague, D.A.: Constraints on the Source Components of Lavas Forming
1334 the Hawaiian North Arch and Honolulu Volcanics, *J. Petrol.*, 44, 603–627,
1335 <https://doi.org/10.1093/petrology/44.4.603>, 2003.
- 1336 Yoshino, T., Matsuzaki, T., Yamashita, S. and Katsura T.: Hydrous olivine unable to account for
1337 conductivity anomaly at the top of the asthenosphere, *Nature*, 443, 973–976,
1338 <https://doi.org/10.1038/nature05223>, 2006.
- 1339 Zakharov, D.O., Tanaka, R., Butterfield, D.A. and Nakamura, E.: A New Insight Into Seawater-
1340 Basalt Exchange Reactions Based on Combined $\delta^{18}\text{O}$ — $\Delta^{17}\text{O}$ — $^{87}\text{Sr}/^{86}\text{Sr}$ Values of
1341 Hydrothermal Fluids From the Axial Seamount Volcano, Pacific Ocean. *Front. Earth Sci.*, 9,
1342 691699, <https://doi.org/10.3389/feart.2021.691699>, 2021.
- 1343 Zhang, F., Lin, J. and Zhan, W.: Variations in oceanic plate bending along the Mariana trench. *Earth*
1344 *Planet. Sci. Lett.*, 401, 206–214, <http://dx.doi.org/10.1016/j.epsl.2014.05.032>, 2014.
- 1345 Zhang, G.L., Chen, L.H., Jackson, M. and Hofmann, A.W.: Evolution of carbonated melt to alkali
1346 basalt in the South China Sea, *Nat. Geosci.*, 10, 229–235, <https://doi.org/10.1038/ngeo2877>,
1347 2017.
- 1348 Zhang, W., Johnston, S. and Currie, C.A., Kimberlite magmatism induced by west-dipping
1349 subduction of the North American plate, *Geology*, 47, 395–398,
1350 <https://doi.org/10.1130/G45813.1>, 2019.
- 1351 Zhang, J., Xu, M. and Sun, Z.: Lithospheric flexural modelling of the seaward and trenchward of the
1352 subducting oceanic plates, *Int. Geol. Rev.*, 62, 908–923,
1353 <https://doi.org/10.1080/00206814.2018.1550729>, 2020.
- 1354 Zhang, G., Wang, S., Huang, S., Zhan, M. and Yao, J.: CO₂-rich rejuvenated stage lavas on Hawaiian
1355 Islands, *Geochem. Geophys. Geosyst.*, 23, e2022GC010525,
1356 <https://doi.org/10.1029/2022GC010525>, 2022.
- 1357 Zhong, Y., Zhang, G.-L., Zhong, L.-F., Chen, L.-H. and Wang, X.-J.: Post-spreading volcanism
1358 triggered by CO₂ along the South China Sea fossil spreading axis, *Lithos*, 404–405, 106478,
1359 <https://doi.org/10.1016/j.lithos.2021.106478>, 2021.

<https://doi.org/10.5194/egusphere-2023-1499>

Preprint. Discussion started: 29 August 2023

© Author(s) 2023. CC BY 4.0 License.



1360 Zindler, A. and Hart, S.: Chemical geodynamics, *Ann. Rev. Earth Planet. Sci.*, 14, 493–571,

1361 <https://doi.org/10.1146/annurev.ea.14.050186.002425>, 1986.